The effect of hydrogen on gas porosity in Laser Powder Bed Fusion of AlSi10Mg

A Thesis Presented for a

Master of Science

Degree

The University of Tennessee, Knoxville

Travis A. McFalls

August 2018

Dedication

For my wife Simona, daughter Olivia, and family.

Acknowledgements

I would like to thank Dr. Alex Plotkowski, Prof Suresh Babu, Jonaaron Jones, Derek Morin, Title 3, Aerojet Rocketdyne, The Airforce, Shaun Buckley, Devon Burkel, Avinash Prahbu, Kevin Lamb, Mike Boice, Joshua Mccoy, and Jacob Raplee.

Abstract

The density of components built using selective laser melting systems are greatly affected by pore formation during rapid solidification. By limiting the hydrogen content of the AlSi10Mg powder and the solidification through build parameters, gas porosity can be reduced. In this study, three types of porosity were characterized in AlSi10Mg samples built by both SLM and Concept Laser systems. Trends relating to energy input and pore type were established for gas, keyhole, and lack of fusion. The physical mechanisms for each type of pore formation were rationalized relative to solidification parameters such as, thermal gradient and solidification front velocity. Areal and volumetric density values were compared for samples built with specific techniques for eliminating hydrogen. The hydrogen content of both powders and builds were analyzed. This measured content confirmed the effectiveness of reducing gas porosity through process parameter control. Finally, the evolution of hydrogen concentrations is evaluated during solidification and the nucleation of gas pores is discussed.

Table of Contents

Chapter 1 Introduction 1

Chapter 2 Background and literature review 2

2.1 Metal additive manufacturing (AM) 2

2.1.1 Governing parameters of L-PBF 3

2.1.2 Scan strategy effects 3

2.2 Previous work with AlSi10Mg in L-PBF 4

2.3 Porosity in L-PBF 5

2.3.1 Lack of fusion pores 5

2.3.2 Keyhole pores 6

2.3.3 Gas pores 7

2.4 Microstructure found in ALSi10Mg 11

2.4 Background summary 12

Chapter 3 Experimental procedure 13

3.1 Sample geometry and processing parameters 13

3.2 Density measurement 16

3.2 Hydrogen measurement 17

3.3 Pre-scanned powder analysis. 17

3.4 Powder feedstock 20

Chapter 4 Results and Discussion 22

4.1 Analysis of raw powder 22

4.2 Analysis of pre-scanned powder 23

4.3 Porosity characterization and morphology 26

4.4 Hydrogen reduction technique 31

4.5 Gas pore mechanisms 40

4.5.1 Hydrogen pore nucleation. 40

4.5.2 Concentration of hydrogen around a dendrite tip due to growth velocity 42

4.5.3 Concentration of hydrogen due to solidification. 45

4.5.4 Hydrogen concentration equilibrium 47

4.5.5 Sources of gas porosity 50

Chapter 5 Future work 53

Chapter 6 Summary and conclusions 54

Bibliography 55
Appendix 59
Vita ..... **Error! Bookmark not defined.**

List of Tables

Table 3.1 Build Parameters for all experimental builds 13

Table 3.2 Chemical Composition of AlSi10Mg powder 21

Table 3.3 Powder Size Distributions 21

Table 3.4 Powder Size Distribution at Micron Leve 21

Table 4.1 Hydrogen concentration in new and used powders 22

Table 4.2 Volumetric Energy Density for each Characteristic Cube 26

Table 4.3 Input Parameters for Rosenthal Simulation 27

Table 4.4 Pycnometer Density measurements REC samples 31

Table 4.5 Optically measured areal density REC samples 32

Table 4.6 Pycnometer readings of all samples produced on the SLM 280 System 36

Table 4.7 Optically measured Density 36

Figure 4.8 Hydrogen concentrations from both REC and 51 samples 37

List of Figures

Figure 2.1 Example of LOF pores found in L-PBF (XY) 5

Figure 2.2 Representation of insufficient weld pool overlap 6

Figure 2.3 Etched sample displaying both conduction mode and keyhole mode melting and displaying resulting keyhole pores 7

Figure 2.4 Gas Porosity 10

Figure 2.5 Phase Diagram of the Aluminum Hydrogen system 10

Figure 2.6 Microstructural solidification mode as a function of R (Solidification velocity) and G (Thermal Gradient) 12

Figure 3.1 Rectangular Bars printed on Concept Laser system. Two Bars with pre-scan and two without 14

Figure 3.2 A different view of the REC samples made on the concept laser system 14

Figure 3.3.1 Raster scan strategy 15

Figure 3.3.2 Stripe scan strategy 15

Figure 3.4 Sectioning methods of Rectangular cubes produced by both SLM and Concept Laser System 16

Figure 3.5.1 Stitched Micrograph red box indicates cropped region for analysis 17

Figure 3.5.2 Cropped and threshold image used for particle analysis 17

Figure 3.6 Partially sintered powder before extraction inside the build chamber 19

Figure 3.7 Partial sintered powder after extraction by the metal grate 19

Figure 4.1 Mounted new powder used in Concept Laser system 23

Figure 4.2 Powder size distribution between new and pre-scanned powders 24

Figure 4.3 Optical micrograph of pre-scanned powder sample 25

Figure 4.4 Temperature Profile based on Rosenthal Calculations of LOF parameters 28

Figure 4.5 XZ micrograph of LOF cube 28

Figure 4.6 Example of Keyhole Porosity (XY) 29

Figure 4.7 Gas Cube Micrograph Displaying small spherical Gas porosity 30

Figure 4.8 Micrographs of all REC samples. Samples 1 and 2 were created with the Pre-Scanning Technique 32

Figure 4.9 Areal Count of Micron Size Pores in the XY micrographs of all REC samples 33

Figure 4.10 Areal count of micron size pores in XZ REC micrographs 34

Figure 4.11 Stitched micrographs of samples produced on the SLM 280 Samples 51AP and 51BP were created using the Pre-Scanning Technique 38

Figure 4.12 Areal Density of the XY micrographs of all samples produced on the SLM 280..... 39

Figure 4.13 Different mechanisms for gas bubble generation within L-PBF process..... 40

Figure 4.14 Gas bubble nucleation at the solidification front 41

Figure 4.15 Solidifying dendrites 42

Figure 4.16 Dimensionless Temperature profile around the dendrite tip..... 43

Figure 4.17 Hydrogen Concentration fields around the dendrite tip at two different Peclet numbers 44

Figure 4.18 Hydrogen supersaturation in the liquid in-front of the solidifying dendrite tip..... 45

Figure 4.19 Scheil diagram for the AlSi10 alloy 46

Figure 4.20 Increasing Hydrogen concentration between the Dendrite Tips..... 47

Figure 4.21 Equilibrium Hydrogen Concentration as a function of fraction solid and initial pore radius 49

Figure 4.22 Equilibrium and inter-dendritic liquid Concentrations compared..... 49

Figure 4.23 Etched Micrograph of Gas pore cube from chapter 4 (XZ direction) 51

Figure 4.24 Higher Resolution image of figure 6.11 displaying gas pores of various sizes..... 52

Chapter 1 Introduction

Additive Manufacturing (AM) is an ever-expanding field concerning both metal and composite components. Adoption of AM methods is growing yearly, and its ability quickly manufacture complex geometric parts adds to its usefulness toward industrial application. Rapid prototyping results from the ability of AM to quickly manufacture parts from a computer aided design (CAD) model. In this process, software is used to take a 3D model and "slice" it into individual 2D drawings. From there, material is either melted, in the case of Powder Bed Fusion (PBF), or deposited according to each slice's geometry. This layer by layer approach builds in the Z direction with the current slice being represented in X and Y. This method of manufacturing allows for the creation of complex geometric shapes with minimum feature sizes as small as 100 microns[1]. In contrast to traditional subtractive manufacturing, were the part is machined out of a solid block of material, the AM approach leaves little wasted material[2]. While this may not be suitable from some products, when it comes to high priced metals, the reduction in waste leads to an increased buy to fly ratio. The buy to fly ratio is the weight ratio between the part itself and the raw material used in its manufacturing process.

While there are several methods to fabricate parts additively, this work will focus on laser powder bed fusion (L-PBF). During this process each layer is bonded to the one below by the laser melting of metal powder. This technology has led to innovative design methodology for additively manufactured components. One specific design for AM tool is the software simulation known as topology optimization (TO). TO uses a finite element analysis (FEA) to eliminate non-loadbearing material from a parts geometry. However, FEA relies on fully dense parts and porosity defects can negatively impact the resulting optimized geometry. The goal of this work is to understand the formation of porosity in AlSi10Mg components built through L-PBF. Specifically, it will focus on Lack of Fusion (LOF), Keyhole, and gas porosity. Each defect was analyzed with respect to the solidification conditions resulting from input parameters of the L-PBF process and a deeper study has been done on the differing mechanisms of gas porosity morphology.

Chapter 2 Background and literature review

This chapter will discuss background of relevant processes and information used in this study along with the corresponding previous work that is found in literature. Section 2.1 will discuss the laser powder bed fusion process, governing parameters, effects of scan strategy, and previous work attributed to parameter development. Section 2.2 will discuss previous work with the aluminum alloy AlSi10Mg. Section 2.3 will address three specific types of defects found in additively manufactured metals and connect them defects found in both the casting and laser welding process. In Section 2.4 an examination of the microstructures found in published literature of AlSi10Mg will be discussed.

2.1 Metal additive manufacturing (AM)

Within metal AM is the method of Powder Bed Fusion (PBF), where metal powder is evenly spread across a substrate and melted according to a specific geometry, with the use of either a laser or electron beam. The lasers are controlled using mirrors and lenses to scan over each layer's or slices' s designated melt area[1]. This process takes these geometric slices of the desired part and builds layer by layer until the part is complete. Each layer is bonded to the layer below through a laser melting process, and the thickness of the layer varies from 10 to 50 micron[1]. At the beginning of each layer, metal powder is spread on the substrate using a powder hopper and a recoater blade. This blade ensures an even distribution of the powder thickness.

The initial layer is fused to a metal plate, usually of a similar material as the powder feedstock, to support the part. In many cases the parts are built upon supports or support material is used where overhangs are present. After the build is complete, the un-melted powder is sieved to remove any partially sintered particles. The complete parts are then cut off the build plate and if needed post processing is then done.

During L-PBF, melt pools are generated at each layer and are sometimes transient in nature [3]. The input parameters, material characteristics, geometry, and scan strategy can each affect the size, shape, and solidification conditions of these weld pools. Therefore, the weld pool characteristics play a significant role in porosity formation and must be further understood in order to characterize the porosity mechanisms.

2.1.1 Governing parameters of L-PBF

L-PBF (laser powder bed fusion) machines differ according to the manufacture, however each consists of a set of similar processing conditions. These conditions control the amount of energy used to melt and fuse each powder layer to the one below. The parameters consist of laser power P (W), scanning speed v (m/s), hatch spacing h (mm), layer thickness t (mm), and spot size S (mm). Previous work has shown how a volumetric energy density E (J/mm^3) (see equation 1) can be calculated based upon these parameters and [4], [5].

$$E = \frac{P}{vht} \tag{1}$$

The energy density associated with a specific set of parameters has also shown to control the shape and size of across the layers weld pools[4]. At lower energy densities these pools do not over lap and un-melted powder is left and, in most cases, leads to lack of fusion porosity. Energy densities too high create weld pool instabilities where molten metal is vaporized and a gas bubble is trapped[6]. Issues with the use of a volumetric energy density to understand the thermal characteristics reduce the effectiveness of this approach. These include the lack of consideration of both the conduction in the weld pool and the laser absorptivity of the powder. While this thesis will not encapsulate an exhaustive parameter optimization, the effects of a range of energy densities (22 to 200 J/m^3) on these types of porosities will be shown. Further investigation of defect mechanisms will be talked about in section 4 of this paper.

Along with energy density is the solidification parameters of thermal gradient G (K/m) and solidification front velocity R (m/s). The thermal gradient expresses both the rate and direction of temperature change at a specific point and the solidification velocity describes the rate at which a liquid is solidifying at the solid liquid interface. Ranges predicted in literature from simulations of laser melted AlSi10Mg include thermal gradient values up to $1x10^7$ (K/m) and solidification velocities up to 1.5 (m/s)[7]. These parameters will be discussed in greater detail in the AlSi10Mg microstructure review.

2.1.2 Scan strategy effects

Although the energy density has considerable control over defect formation, the scan strategies, by which each layer is melted, can influence localized pore growth and defect generation[8], [9]. The scan strategies employed in L-PBF consist of raster, stripe, or some variation and is describe as the method by which the laser moves along the part's geometry during melting. The raster strategy

meanders the laser back and forth across the entire part until that layer is melted. The stripe pattern divides each layer into sections and rasters the laser through each section. These melting strategies can cause differing thermal trends within the same part and impart large thermal gradients that will influence thermal stresses and defects[10][11]. Kruth showed that by reducing the length of scan vectors could decrease thermal gradients and lessen thermal stresses within a part[11].

2.2 Previous work with AlSi10Mg in L-PBF

A significant amount of research can be attributed to AlSi10Mg alloy in the selective laser melting process[8], [12]–[19]. AlSi10Mg was originally developed as a casting alloy and has a high thermal conductivity (113 W m^{-1} K^{-1})[20]. Previous researchers selected this alloy for it good weldability while maintaining good strength and hardness[8], [13]. The weldability is attributed to the near eutectic composition which decreases the solidification range from that of other aluminum alloys [12].

The use of aluminum powders in L-PBF do present several challenges. Louvis et al described the issues of moisture on the powder and its effects on the flowability leading to blockages in the feed and distribution systems[12]. Aluminum powder has a high reflectivity and with the high thermal conductivity of solid material, Buchbinder et al discussed the need for higher laser powers to ensure complete melting[19]. The presence of aluminum oxides (Al_2O_3) both the powder, liquid, and solidified surface require high laser powers to dissipate and the intersection of oxide films may cause porosity[12]. In casting, oxides on the surface of the molten material may be mixed due to turbulent fluid flow and result in localized reduced mechanical properties and pore formations[21].

2.3 Porosity in L-PBF

Three types of common pores found in L-PBF are lack-of-fusion, keyhole, and gas, and each has distinct mechanism of materialization and possible growth. The next three sections will discuss each type of pore with respect to the published literature. Previous modeling efforts of the formation or growth of porosity will be reviewed.

2.3.1 Lack of fusion pores

Lack of fusion (LOF) porosity arises from regions of non-melted powder encased in the solid part. It has been shown that LOF pores occur at the intersection of weld pools of the same layer and that it stems from deficient connection between these pools[4], [22]. The morphology of this type of porosity has been thoroughly described in welding and L-PBF literature[22], [23]. An example of a LOF pore found in additively manufactured AlSi10Mg can be seen in figure 2.1.

Figure 2.2 shows two examples of where LOF pores can form. Inadequate horizontal weld pool overlap leading to interlayer pores can be seen in figure 2.2.1. The presence of LOF porosity can produce poor interlayer bonding and rough surface finishes[22]. The occurrence of LOF pores has proved to be mostly avoidable by increasing the weld pool size and ensuring adequate weld pool overlap[15].

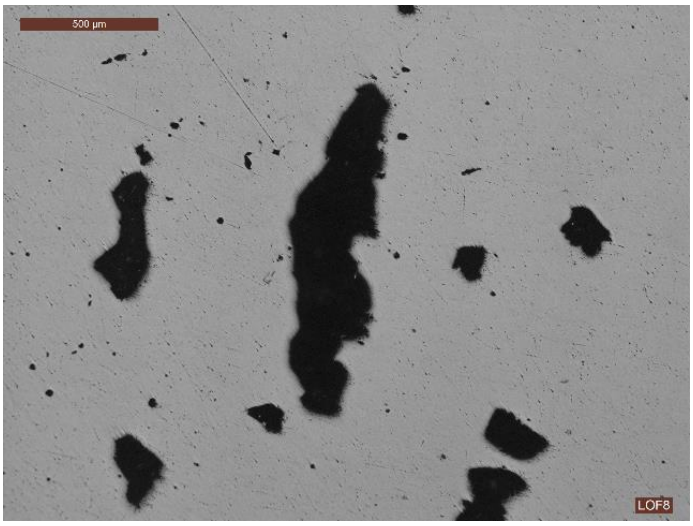


Figure 2.1 Example of LOF pores found in L-PBF (XY)

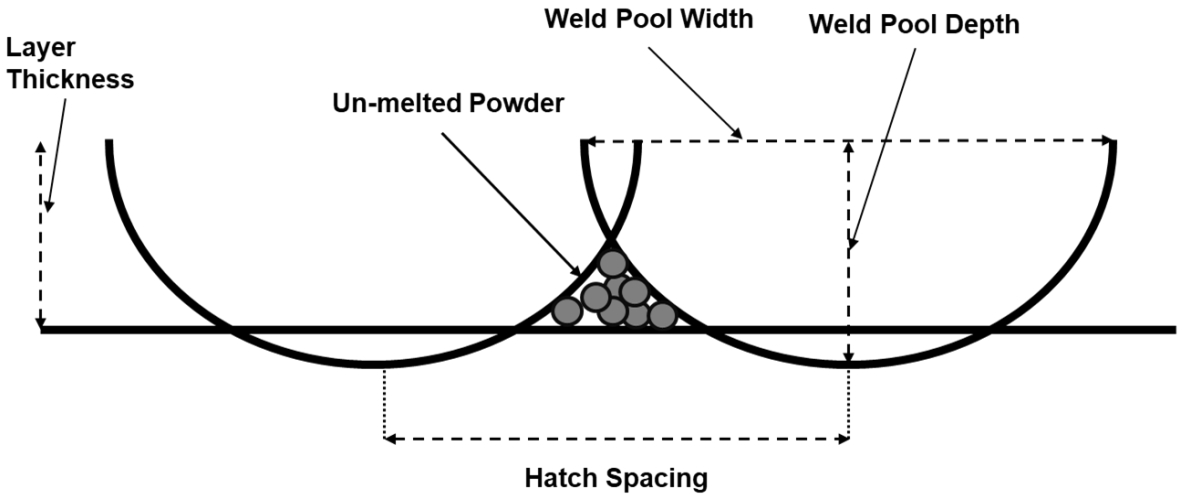


Figure 2.2 Representation of insufficient weld pool overlap

Extensive work has been done in the prediction of LOF pores [4]. It was shown that the size and shape of each weld pool is controlled by the energy density based upon a specific set of input parameters. Insufficient weld pool width, depth and hatch distance can all contribute to the formation of these defects and the lower energy densities are attributed to them [4]–[6]. Therefore, a transition from lack of fusion to fully melted material exists based upon an increase in overall weld pool shape and size, however some limitation does apply. Tang showed that different combination of power and velocity can result in differing amounts of predicted porosity for the same energy density[4].

2.3.2 Keyhole pores

A common phenomenon in both laser welding and L-PBF is the development of a deep penetrating weld pool due to keyholing. This happens when a deep hole is formed in the molten metal by high energy density input from the laser beam. This high input energy creates powerful recoil pressure by evaporating the liquid metal and creating a vapor cavity that allows for increased absorption of the laser beam. This increased energy absorption cause the weld pool to deepen further than possible during conduction mode melting[24], [25]. While, in welding, stable keyhole-mode melting can result in favorable deep weld pools penetrating into the base materials, unstable keyholes can produce pores due to metal vapor bubbles trapped by solidification[24], [26]. When high enough energy densities are utilized in L-PBF keyhole pores can form throughout the part and greatly reduces

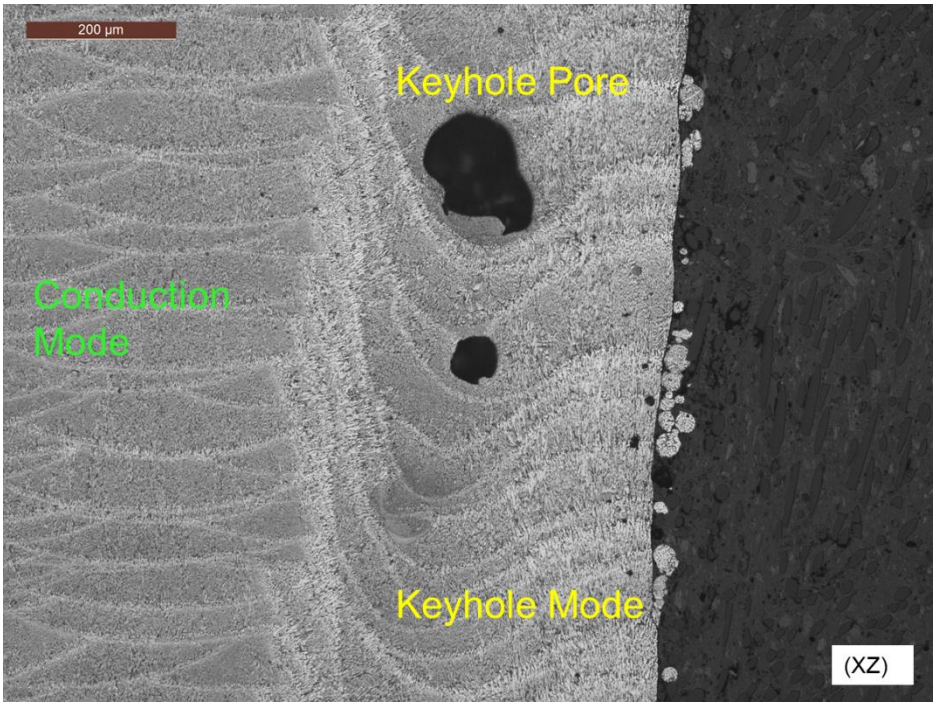


Figure 2.3 Etched sample displaying both conduction mode and keyhole mode melting and displaying resulting keyhole pores

the overall density[27]. An example of a keyhole pore can be seen in figure 2.3. These pores generally include gases with respect to the shielding gas or in the case of PBF the operating environment.

In the L-PBF process layer by layer melting can cause over heating at certain locations based on a combination of geometry and scan strategy. The resulting melt pool size and shape are not always continuous along the length of a weld and can change through the build height and geometric location [8] and the scan strategy utilized can greatly impact these characteristics[9]. The shape of keyhole pores tends to be somewhat spherical due to the morphology and the size is generally relative to the melt pool. Avoiding formation of these pores is attainable by reducing the energy density imparted to each layer[27].

2.3.3 Gas pores

Gas porosity occurs when a gas bubble is trapped by the solidification front, however the formation of this bubble varies due to certain mechanisms. Current L-PBF literature discusses three ways in which gas pores form[18], [28], and this topic has been widely discussed with respect to casting[29]. Gas bubbles can result from both porosity present in the powder and entrapped gases due to weld pool instabilities[16]. The turbulent nature of the fluid flow in the weld pools cause gases to

become entrapped, like a wave crashing against the shore of the ocean. These gas bubbles can then be carried by fluid flow and finally trapped by the solidifying metal. Likewise, gas pores present in the powder when melted can be carried and trapped in the same manner. The rapid solidification during the L-PBF process does not allow time for the gas bubbles to escape. The resulting gas pores have a spherical shape and an example can be seen in figure 2.4.

Specific to the case of Aluminum alloys, is the nucleation of hydrogen pores. This is a well-known phenomenon in casting, welding, and L-PBF literature[18], [30]–[33]. Hydrogen is present in the form of either H_20 on the surface of the powder or saturated in the aluminum crystalline structure. Figure 2.5 of the Al H system clearly shows a significant increase in H solubility between the solid and liquid aluminum phases. Hydrogen present in the solidifying aluminum is rejected into the mushy zone thereby increasing the concentration of H_2 in the liquid phase. The hydrogen concentration in the mushy zone reaches a supersaturation point and a gas bubble nucleates. Once nucleation occurs, diffusion controls the growth of the bubble until trapped by the solidification front resulting in a hydrogen gas pore. Current work shows that hydrogen porosity in L-PBF can be reduced by controlling the amount of hydrogen present at the time of melting. Weingarten et al showed that by drying the powder with either a low power laser pass or baking in an oven would reduce the presence of moisture on the powders surface[18]. In castings an increased cooling has been shown to decrease both pore size and volume fraction[34], however cooling rates as high as $7x10^6$ (K/s) during the L-PBF process which are considerably higher by several orders of magnitude[19].

2.3.3.1 Modeling hydrogen gas porosity

Significant work has been done in modeling the nucleation and growth of hydrogen pores in casting literature[30], [31], [33], [35], [36]. No investigations of nucleation during the L-PBF process have not been conducted, however cooling rates between laser welding and L-PBF are of the same ranges. Most current models do take the solidification parameters into consideration and provide a good basis for future work. Khalazjzadeh et al incorporated the Young-Laplace equation (equation 2) and the ideal gas law (equation 3) to show that changes in gas pore constituent, pressure in the liquid and localized temperature correlated to changes in the pore radius for both nucleation and growth [30].

$$P_p = P_l + P_\sigma \tag{2}$$

Equation 2 relates the pressure in the pore P_p to the sum of the liquid pressure P_l and the capillary pressure due to surface tension P_σ. Because of the spherical shape of the pores $P_\sigma = \frac{2\sigma}{r_p}$ where σ represent the interfacial energy.

$$P_p = \left(\frac{C_{lp} f}{Ke}\right)^2 P_{atm} \tag{3}$$

Equation 3 is Sievert's law which relates the partial pressure of a gas pore in a liquid reservoir to the gas concentration at the solid liquid interface. C_{lp} is the concentration of the gas, Ke is the equilibrium constant for the gas and based on the temperature of the liquid, f is the activity coefficient of the gas, and P_{atm} is the atmospheric pressure. Khalazjzadeh theorized that for a pore to nucleate at a certain initial radius $r_{p,0}$ the following inequality (equation 4) must first be met[30].

$$P_p - P_l \geq P_{\sigma,0} \tag{4}$$

Where $P_{\sigma,0}$ is the capillary pressure associated with $r_{p,0}$ and P_p is calculated by Sievert's Law.

Hans and Viswanathan considered that during directional solidification of Al alloys, macrosegragation of hydrogen was possible due to rejection from the solidifying material[35]. Here rejected hydrogen diffuses through the mushy zone continually enriching the liquid until a critical concentration is met for pore nucleation. Most models do not account for an increase in hydrogen concentration in the liquid as a result of this diffusing in-front of the solidification front and calculate the current concentration based upon the mass balance i.e. lever rule[30], [33]. However Li et al does discuss the implications of macrosegragation upon the critical concentration required for nucleation[31]. Although directional solidification is a very specific solidification mode, generally local directional solidification is used to simulate the conditions at specific points throughout the weld pool in L-PBF.

J. Campbell questioned the underlying theories of nucleation in relationship to the interdendritic shrinkage pressure and pore pressure[36]. He calculates the shrink pressure necessary in the mushy zone for pore nucleation to occur and theorized that homogeneous nucleation of pores was not attainable in castings. Dantzig and Rappaz agree that homogenous nucleation is incapable of taking place based upon the Young-Laplace correlation and suggest that hydrogen concentration as low as 0.1 ppm are sufficient for hydrogen pores to nucleate[37].

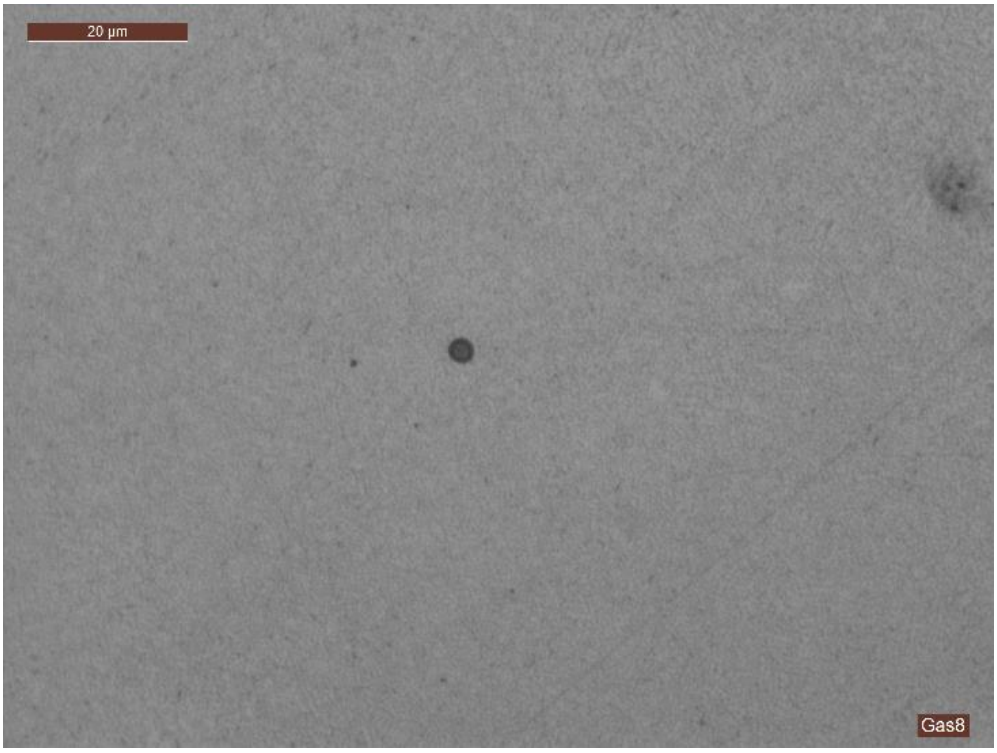


Figure 2.4 Example of Gas Porosity

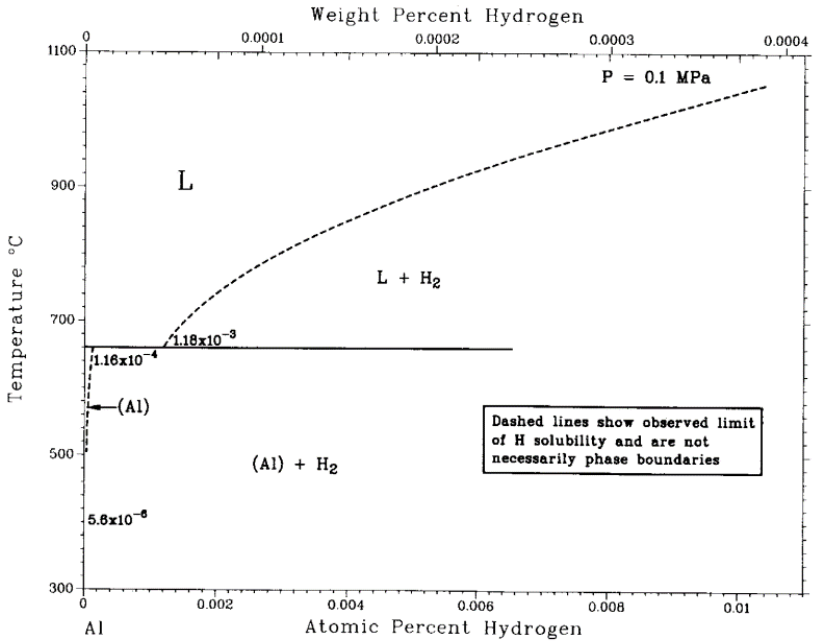


Figure 2.5 Phase Diagram of the Aluminum Hydrogen system.

2.4 Microstructure found in ALSi10Mg

The microstructure of metals made with L-PBF is dependent upon the thermal solidifying conditions and composition of the alloy. The solidifying conditions are dependent on the parameters of solidification rate, thermal gradients, and cooling rate. Plotkowski et al simulated these parameters through the use of an analytical heat transfer model and found that for AlSi10Mg the thermal gradient can be as high as $1X10^7$ (K/m) and solidification rates as high as 1.5 (m/s)[7]. Alloys with differing composition leads to segregation at the solid liquid interface due to diverse solidifying temperatures of independent elements. Three distinct types solidification modes have been observed in welding literature. These include planer, cellular, and dendritic[38]. Figure 2.6 shows the effect of thermal gradient (G) and solidification velocity on the solidification mode[39].

Several investigations of microstructure have been completed for both single track and multilayer builds laser melted AlSi10Mg[8], [14], [19], [40]. Brandl et al showed a heterogenous microstructure size throughout the melt pool and that the rapid solidification produced Al rich cellular dendrites with a Si inter-dendritic phase[14]. A fine cellular dendritic microstructure was also observed by several researchers[8], [40]. Aboulkhair et al concluded that this fine microstructure and homogenous composition throughout weld pools resulted in a higher hardness values leading better mechanical properties than in as-cast metals of the same alloy[40]. The ability to create a sub-micron cellular dendritic fine microstructure was detected by Thijs et al and was attributed to a combination of high solidification rates and thermal gradients[8].

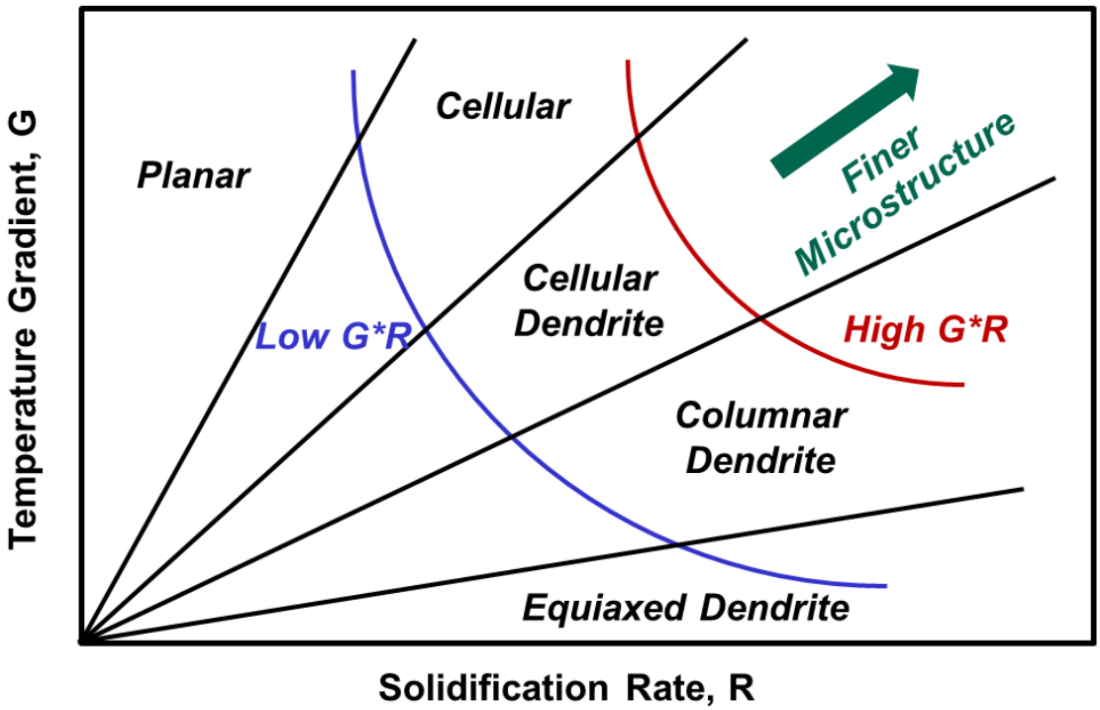


Figure 2.6 Microstructural solidification mode as a function of R (Solidification velocity) and G (Thermal Gradient)

2.4 Background summary

The preceding literature review establishes that during the L-PBF process, weld pool characteristic affect pore formations. LOF porosity emerges from insufficient overlap due to the weld pools size and shape. Keyhole pores can form because of keyhole mode melting which is a consequence of the energy input causing the material to vaporize. Gas porosity was shown to have three distinct mechanism and that in aluminum alloys, hydrogen contamination can lead to the nucleation of gas bubbles. A technique has been developed to reduce hydrogen concentration during the L-PBF process and will be quantified in this body of work. Reconfirmation of the mechanisms that cause LOF, keyhole, and gas pores will be rationalized. Finally, the solidification conditions surrounding the supersatureation of hydrogen will be simulated to give a better understanding of the nucleation of gas pores.

Chapter 3 Experimental procedure

Three separate builds consisting of two sets of four rectangular prisms and three characteristic square cubes make up the additively manufactured experimental parts. The goal of the characteristic cubes was to create an example of diverse types of porosity to characterize the size and shape of each. The rectangular prisms were created to measure the effect of a porosity reduction technique known as pre-scanning.

3.1 Sample geometry and processing parameters

One of the sets of four and the characteristic cubes was built on a Concept Laser Xline 1000 and the other set of four was manufactured on a SLM 280. The set of four built with Xline is denoted as REC and the SLM samples as 51. Both the REC and 51 samples consisted of two cubes built with a pre-scan and two without and the melting scan parameters were kept consistent with respect to the machine they were manufactured on. The dimensions of the rectangular prisms were 25x14x101 mm (width, height, length). The three characteristic cubes were each created to induce the three distinct types of porosity (LOF, Keyhole, Gas) described in section 2 and had dimensions of 19x19x19 mm. Pictures of REC builds can be seen in figure 3.1 and 3.2. The parameters for each set of cubes can be seen in table 1. All samples were built upon supports. For this study only two scan strategies were considered, raster and stripe. The scan pattern consists of the laser meandering back and forth across the entire part as seen in figure 1a. The stripe scan strategy involves the laser rastering back and forth across a "stripe" of the part. The raster pattern was rotated 90 degrees each layer and the stripe pattern 66 degrees.

Table 3.1 Build Parameters for all experimental builds

Build	Laser Power (W)	Velocity (m/s)	Hatch (mm)	Beam Diameter (mm)	Scan Strategy
LOF	1000	2.2	.4	.4	Raster
Gas	1000	2.2	.2	.4	Raster
Keyhole	500	.5	.1	.1	Raster
REC (1,2,3,4)	1000	2.2	.2	.4	Raster
Pre-scan REC (1,2)	70	2.2	.2	.4	Raster
51 (A,B)	NA				Stripe
Pre-scan 51	NA				Stripe

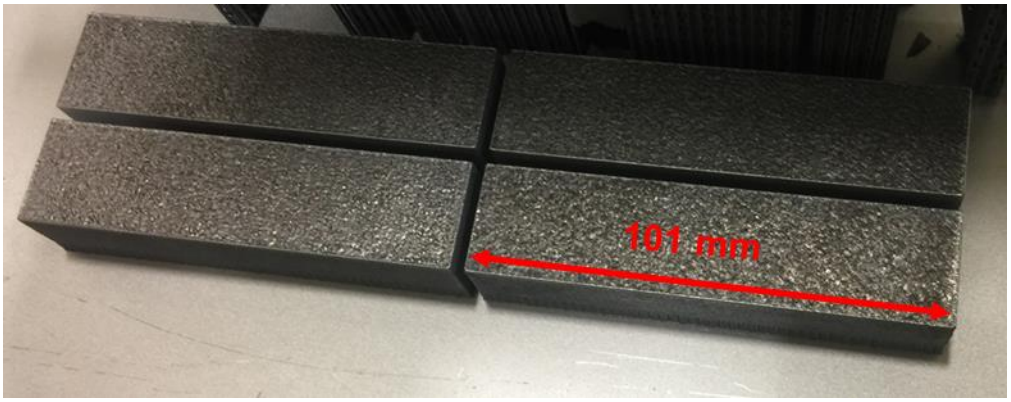


Figure 3.1 Rectangular Bars printed on Concept Laser system. Two Bars with pre-scan and two without.

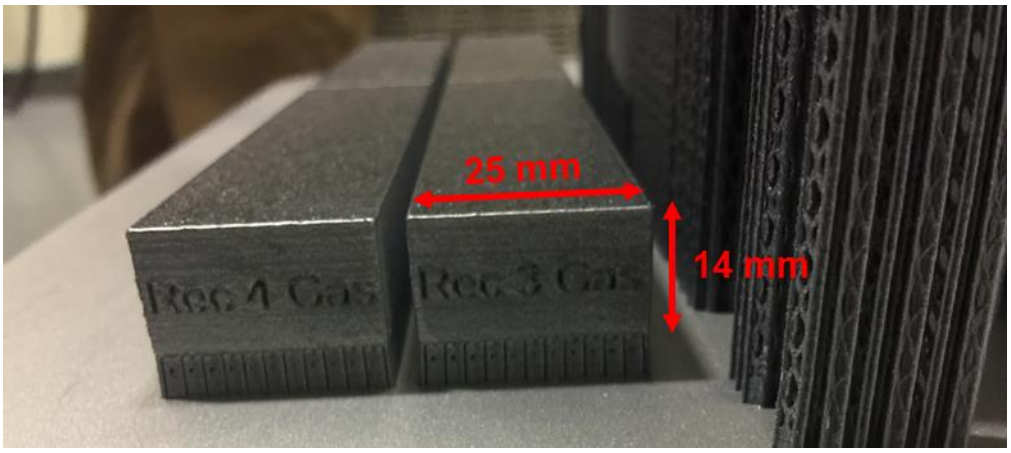


Figure 3.2 A different view of the REC samples made on the concept laser system.

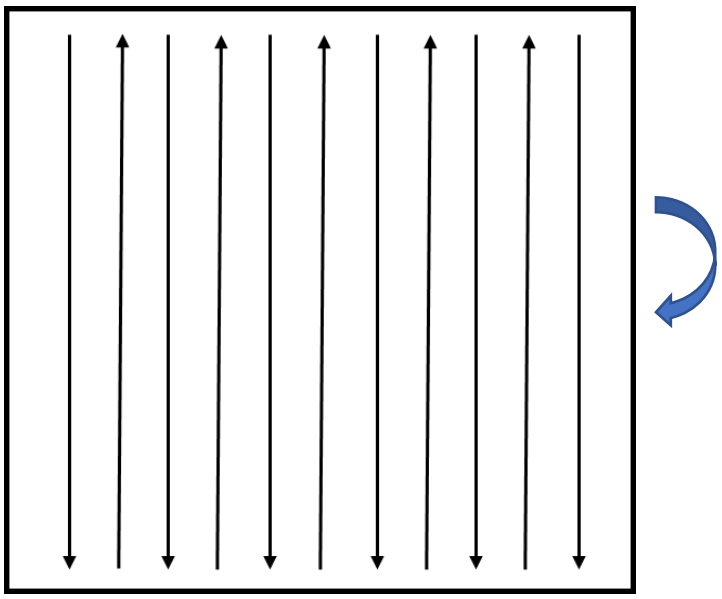


Figure 3.3.1 Raster scan strategy 90 deg rotation each layer (XY)

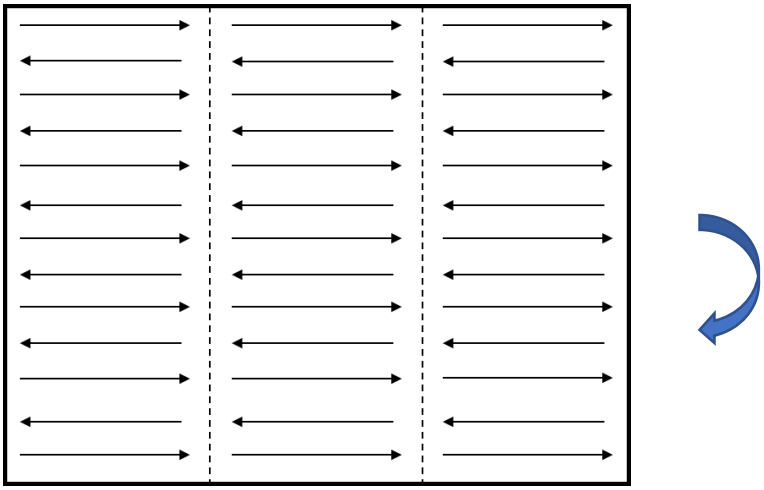


Figure 3.3.2 Stripe scan strategy 66 deg rotation (X,Y) each layer

3.2 Density measurement

Each of the REC samples were sectioned in xy and xz directions, then mounted and polished down to a sub-micron grit. Figure 3.4 shows the sectioning.

Each of the polished samples were examined optically by a Leica dm4000 M LED and stitched images where created for image analysis. ImageJ is image analysis software package that was utilized for the density analysis. By applying contrast filters and setting a threshold, determination between fully dense (white areas) and pores (dark areas) can be analyzed. The software does this by measuring the area of the white and dark areas and identifying distinct particles or in this case pores. An example of the threshold image can be seen in figures 3.5.1 and 3.5.2. The software measures the circularity and area of each pore (dark areas) and outputs them individually in a spreadsheet. In this case the total area of all the pores was used to calculate the percent dense of the solid part and is a 2D areal density. Error can arise from the resolution of each micrograph in comparison to the representative pores. If a pore is smaller than the pixel size error will be induced. Because of this, 9 higher resolution images were taken of each polished sample and had a pixel size of 244 x 244 nanometers. Therefore, analysis of micron size pores was possible.

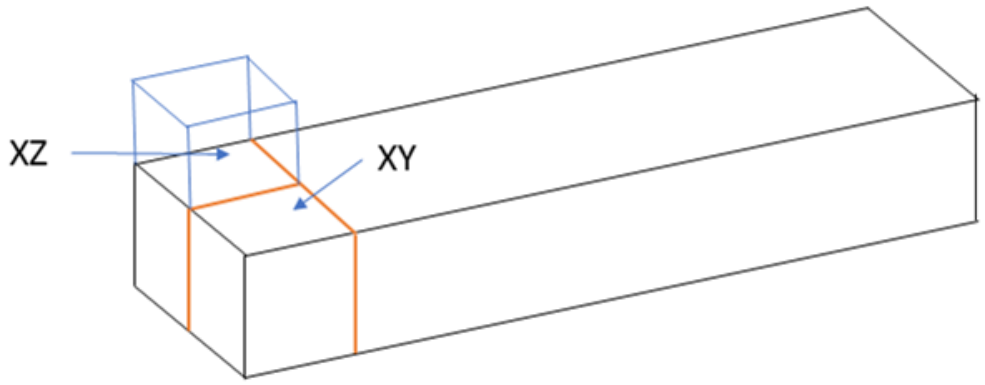


Figure 3.4 Sectioning methods of Rectangular cubes produced by both SLM and Concept Laser System.

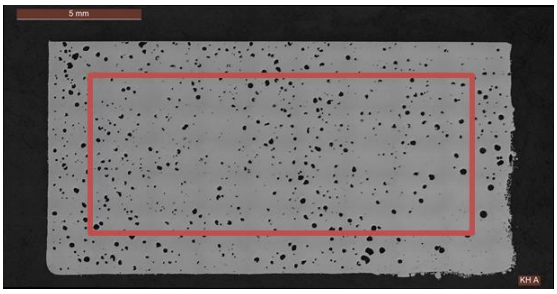


Figure 3.5.1 Stitched Micrograph red box indicates cropped region for analysis

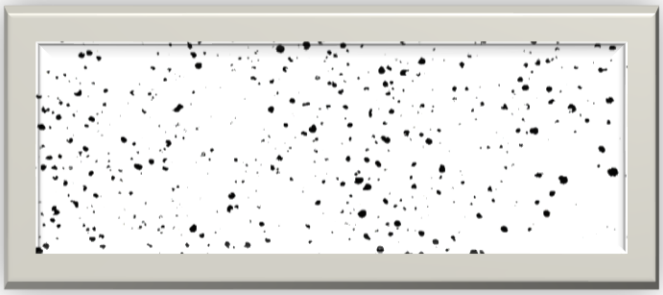


Figure 3.5.2 Cropped and threshold image used for particle analysis

Another section of both the REC and 51 samples was sectioned for pycnometer density measurement. Gas pycnometery was used to measure the volume of the samples. With the measured weight and volume, the true global density could be calculated by equation 5.

$$\rho_s = \frac{W_s}{V_s} \tag{5}$$

Where ρ_s is the density of the sample W_s is the weight of the sample and V_s is the volume. Then by comparing that calculated density to the theoretical density of ALSi10Mg 2.67 (g/cm^3), percent dense value can be calculated. Gas pycnometery utilizes the Archimedes principle except in the place of water, helium is used. This method involves measuring the volume repeatedly until the standard deviation between test is below a set threshold.

3.2 Hydrogen measurement

A section of each REC and 51 builds were analyzed for hydrogen content by inert gas fusion. Along with these, a powder sample from each machine was measured for comparison. The powder samples were taken from both new and recycled powder. Recycled powder refers to powder that has been through a previous build cycle and is sieved for reuse. In the gas fusion process, the sample is melted, and water vapor is measured through infrared detection (ASTM E 1447-09). The results are reported in parts per million (ppm) by weight with an error of +/- 2 ppm.

3.3 Pre-scanned powder analysis.

Another experiment was conducted to measure the efficiency of drying the powder with the laser. Here a large spare area was scanned at the lower power. Before this took place, a metal grate was place

several layers below the top layer of powder and slowly lifted out as to only capture the partial sintered powder of the top layer. The powder can be seen in figure 3.6 before retrieval and in figure 3.7 after removal. Powder was also removed from the same batch that had not been laser scanned for a comparison. Samples from the pre-scanned powder along with new powder were mounted and polished for optical examination. Finally, the powder size distributions were measured with the use of a Malvern Morphologi G3 Se for particle analysis.

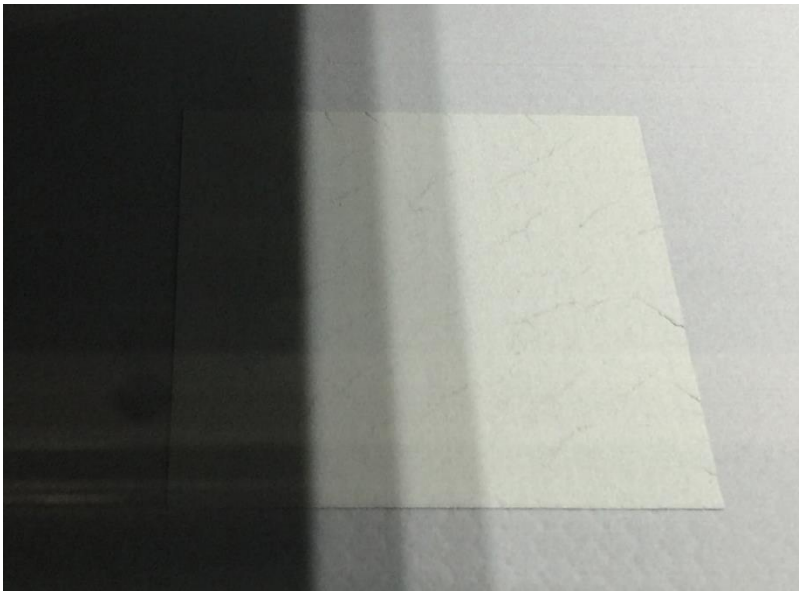


Figure 3.6 Partially sintered powder before extraction inside the build chamber

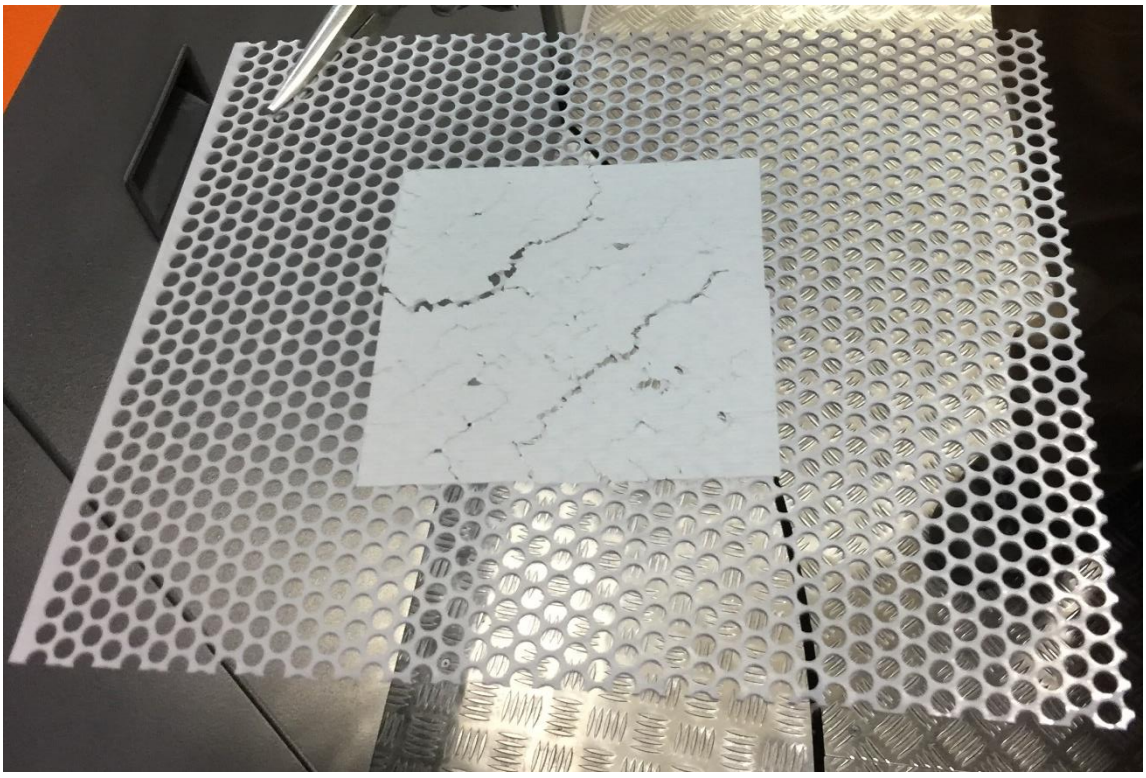


Figure 3.7 Partial sintered powder after extraction by the metal grate

3.4 Powder feedstock

The chemical analysis of the AlSi10Mg powder can be seen in table 3.2 and is comprised of the base metal aluminum. This powder was used in the concept laser system.These test results were obtained by Valimet, Inc using inductively coupled plasma optical emission spectrometry. Inductively couple plasma is used to stimulate atoms and ions thereby emitting electromagnetic radiation unique to an elements wavelength[41].

A sieve analysis was used to determine the particle size distribution of the AlSi10Mg powder. The results of the analysis can be seen in table 3.3. As measured 90.8% of the powder was smaller than the 325-sieve number which corresponds to a sieve opening of 44 microns. Further particle size test was done using a Microtrac system and the results can be seen in table 3.4.The D values (10,50,90) represent the intercepts of the particle sizes at 10%, 50%, and 90% of the cumulative mass. The D50 measurement is the diameter at which 50% of the sample's mass is the comprised of particles with a dimeter less than 29.91 µm.

Table 3.2 Chemical Composition of AlSi10Mg powder

Element	Weight %
Al	Balance
Mg	.3
Cu	.03
Fe	.17
Mn	.05
Si	10.45
Ti	<0.01
Zn	0.01

Table3.3 Powder Size Distributions

Sieve Number	% by weight
+200	0.2
+270	1.6
+325	7.4
-325	90.8

Table 3.4 Powder Size Distribution at Micron Level

Size	Value
D10	15.47 µm
D50	29.91 µm
D90	50.58 µm

Chapter 4 Results and Discussion

4.1 Analysis of raw powder

Hydrogen contamination is aluminum alloys were shown to be a source of gas porosity in both welding and L-PBF processes. As discussed in chapter 2 the source of hydrogen can from both moisture on the surface of the powder or trapped in the solid aluminum. To understand the concentration in the raw powder samples were taken from both machines utilized and the total hydrogen content was measured by inert gas fusion. The results can be seen in table 4.1 and show that powder that had been used during the build process trended lower than that of new powder. This drop is attributed to the powder being dried by the 200 deg Celsius operating temperature for both build chambers.

Further analysis was done on the new powder from the concept laser system, were it was mounted and polished for optical examination. Figure 4.1 displays a micrograph of this powder and small spherical pores can be seen in several of the particles. It is not known whether these pores are hydrogen gas pores or are gas pores resulting from the inert gas used during the powder making process. What is known is that these pores are of a micrometer scale and that if they are the result of nucleating hydrogen bubbles then supersaturation must be taking place during the gas atomization process. In this process inert gas is infused into a jet of molten metal to created spherical powder particles for the use of powder metallurgy applications such as L-PBF. Inquiry was made into how the specific process works and it was found that once completed the atomized powder was exposed to local environment. It was theorized that a source for the moisture on the powder surface could be a consequence of this exposure if humidity was present in that environment.

Table 4.1 Hydrogen concentration in new and used powders

Sample (AlSi10Mg)	Hydrogen Content ppm	Hydrogen cc/100g	+/- PPM
SLM Used	21	23.52	2
SLM New	24	26.88	2
Concept New	39	43.86	2
Concept Used	35	39.2	2

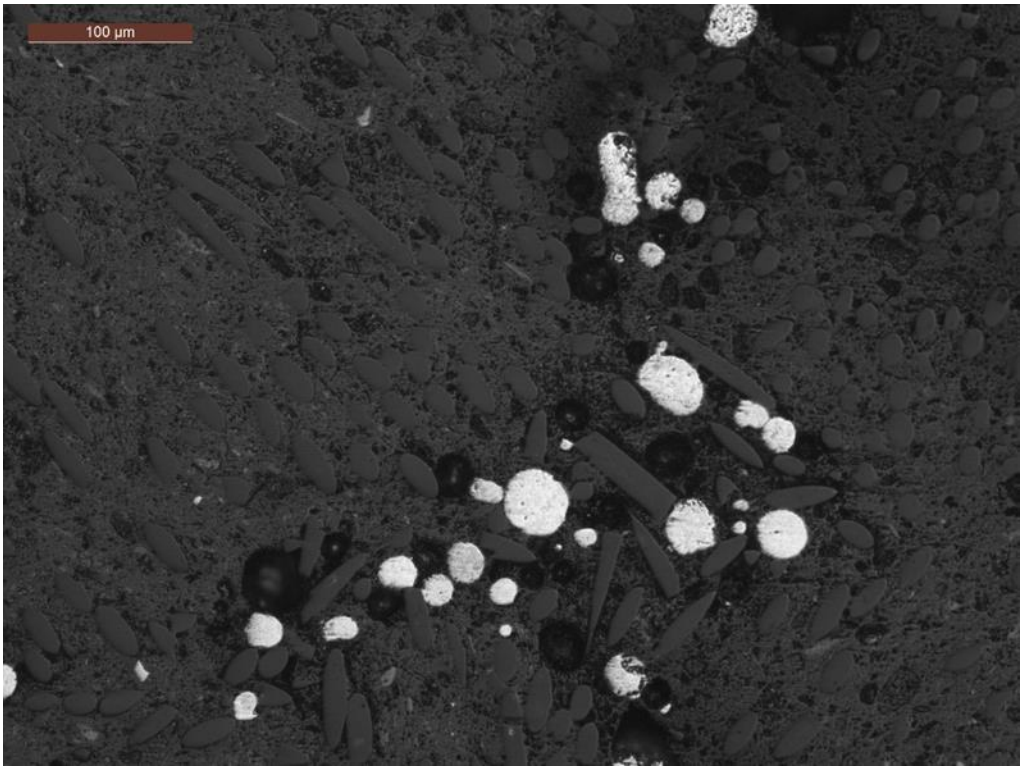


Figure 4.1 Mounted new powder used in Concept Laser system

4.2 Analysis of pre-scanned powder

As discussed in chapter 2, a technique was developed by Weingarten et al to pre-scan the powder before each layer was melted to reduce hydrogen concentrations during the build[18]. To understand the effect of the pre-scanning a sample of pre-scanned powder was made as described in section 3.3. The size distribution between the new powder and the pre-scanned powder can be seen in figure 4.2. The size of the pre-scanned powder trends higher than that of the new and is a result of powder particles that have been partial sintered.

For further analysis a sample of the pre-scanned powder was mounted and polished. A representative optical micrograph can be seen in figure 4.3. Notice that now there is a presence of larger pores than observed in the new powder micrograph figure 4.1. It was theorized that three different mechanism may be causing the formation of these larger pores. The first is that these pores are an artifact of were several particles sintered together. During polishing a sintered particle could be removed from this cluster and the result would look like a porosity. However, if that is the case, these pores should look more like a LOF porosity instead of the spherical shape. The second theory put forth

is that hydrogen within the particle could coalesce and grow the micro pores observed in figure 4.1. Under the assumption that the pre-scanning pass does not melt the material this would require solid state diffusion through the solid aluminum and literature suggest that the diffusion constant of hydrogen would be $1.1x10^{-5}$ (m^2/s)[42]. The third theory is based upon the ideal gas law were the gas inside the pore is heating up due to the laser pass and expansion of that already present pore is happening. Without knowing the composition of the gas inside the pore it is not possible to know whether it is being formed from hydrogen coalescence or expansion of a present pore. In previous work it has been shown that during long heat treatment cycles expansion of pores can happen[18].

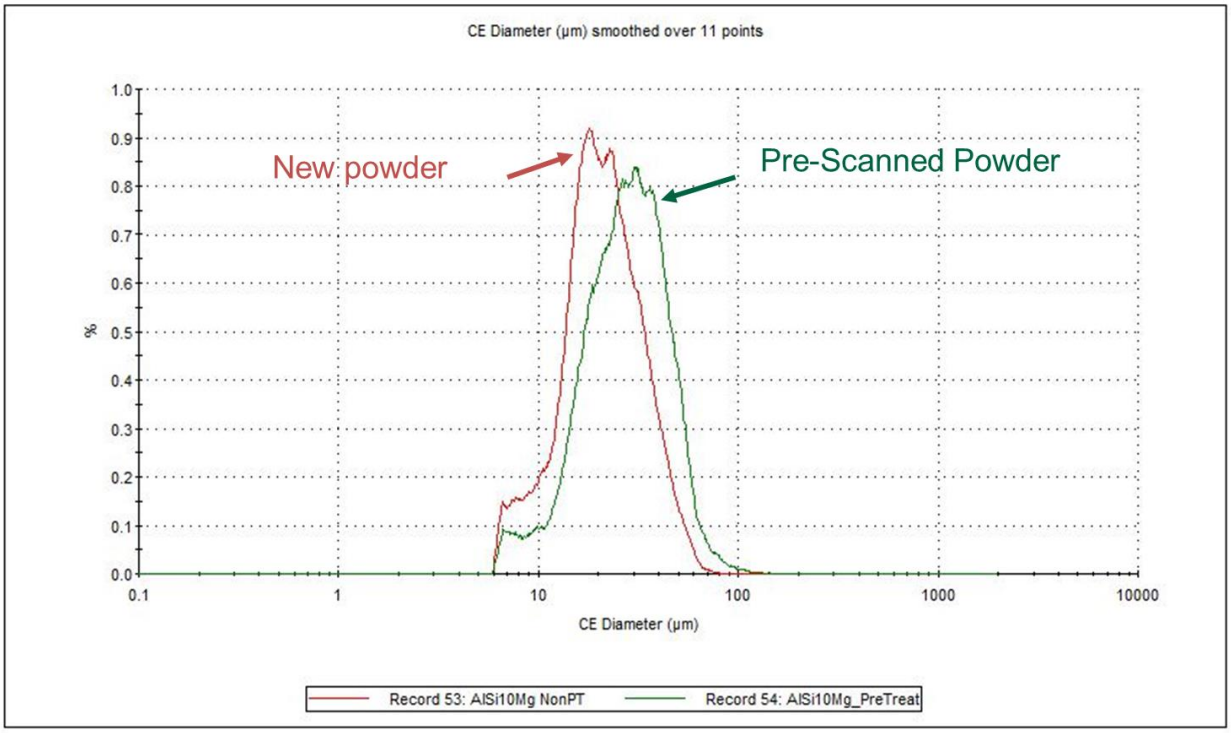


Figure 4.2 Powder size distribution between new and pre-scanned powders

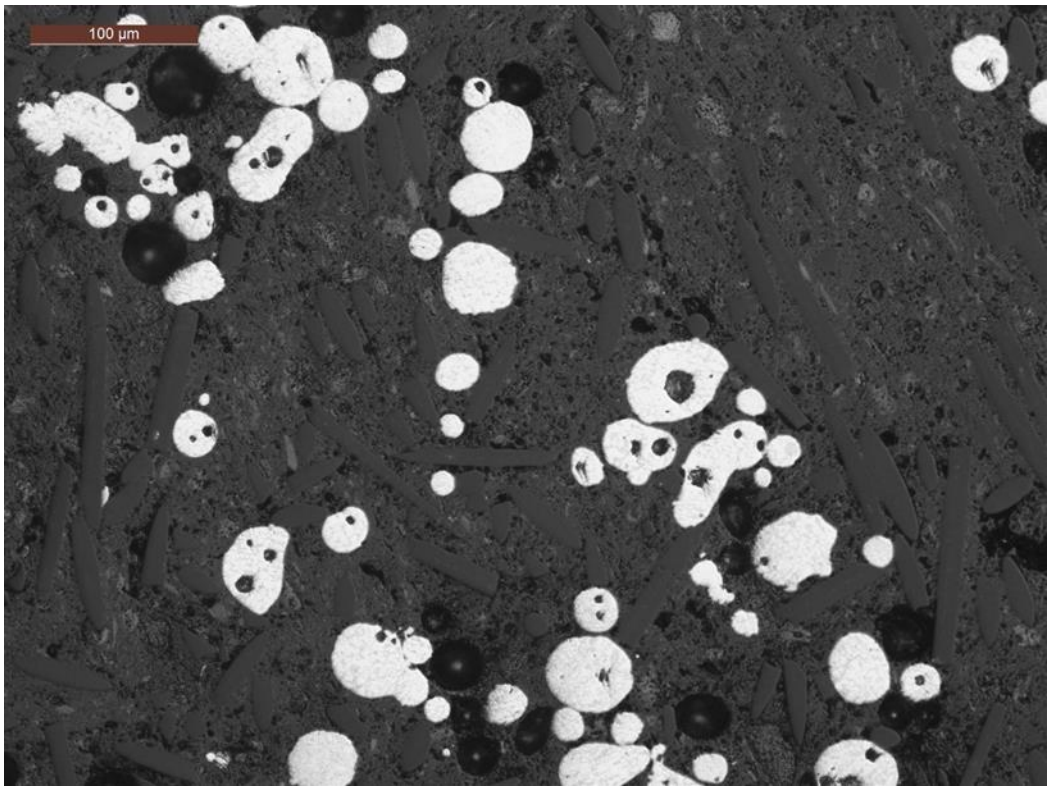


Figure 4.3 Optical micrograph of pre-scanned powder sample.

4.3 Porosity characterization and morphology

As discussed in the background section three specific types of porosity are common in L-PBF: keyhole, gas, and lack-of-fusion. This section will compare the specific parameters that were used to induce the pores. The resulting energy density from each parameter set is used to set regions with respect to the type of porosity.

Table 4.2 displays the associated energy density relative to the type of porosity produced. The goal with this set of builds was not to map out regions where each type of porosity formed with respect to the energy density, but to make sure that each kind was produced. Therefore, giving many examples of each type of porosity to optically examine.

The morphology of lack of fusion stems from insufficient weld pool overlap as discussed in section 2.3.1. This was accomplished for this build by increasing the hatch spacing from 200 micrometers to 400 micrometers. To understand the width of the weld pool under these parameters the Rosenthal equation for a moving point heat source was used[43], [44]. Equation 6 shows the temperature distribution for a thin plate with a moving

heat source at a constant velocity.

$$T(x,R) = T_o + \frac{q}{2\pi k}\left(\frac{1}{R}\right)e^{\left[-\frac{v}{2a}(R+x)\right]} \quad (6)$$

Where T_o is the initial temperature, q (J/m) is the absorbed power, k (W/mK) is the thermal conductivity, v (m/s) is the velocity of the heat source, a is the thermal diffusivity (m/s), and R (m) is the radial distance from the beam location $R = \sqrt{x^2 + y^2 + z^2}$. In this case the absorbed power q is the lasers input power and the simulation does not consider absorptivity of the metal powder or the effects of the laser's profile. Table 4.3 shows the input parameters for AlSi10Mg.

Table 4.2 Volumetric Energy Density for each Characteristic Cube

Energy Density (J/mm^3)	Type of Porosity
22.72	Lack of Fusion
45.45	Gas
200	Keyhole

Table 4.3 Input Parameters for Rosenthal Simulation

Property	AlSi10Mg
Solidus Temperature (K)	850.0
Liquidus Temperature (K)	869.0
Density (kg/m^3)	2670
Specific Heat (J/kg-K)	920
Thermal Conductivity (W/m-K)	175

The resulting temperature distribution in the x and y direction for the lack-of-fusion parameter set can be seen in figure 4.4. The melt pools width is calculated to be around 500 micrometers. However, with a hatch spacing of 400 micrometers, sufficient overlap did not occur. This resulted in LOF porosity throughout the cube. Figure 4.5 displays a micrograph of the LOF cube produces. In this case it was observed that the hatch spacing was set too high and large lack-of-fusion zones resulted.

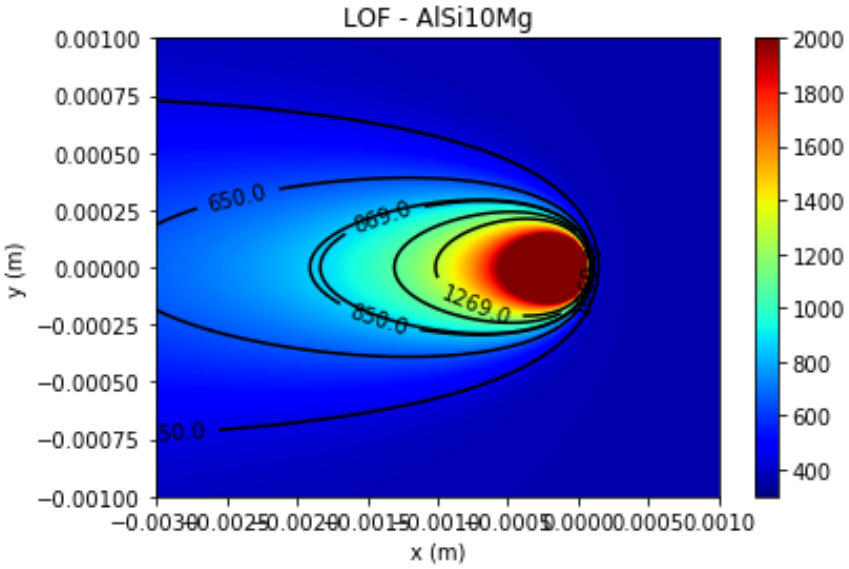


Figure 4.4 Temperature Profile based on Rosenthal Calculations of LOF parameters

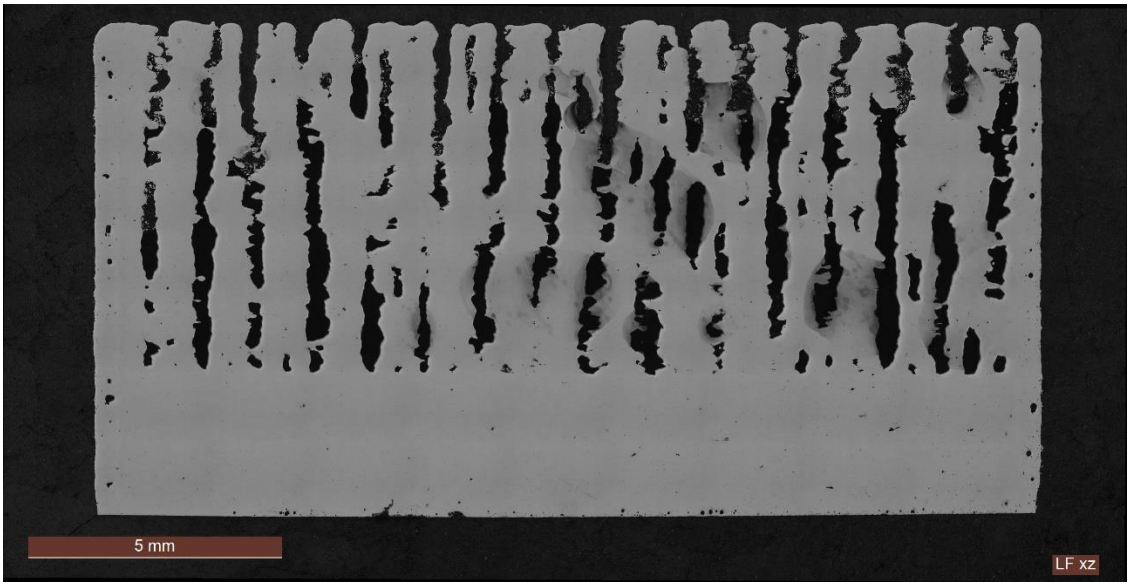


Figure 4.5 XZ micrograph of LOF cube

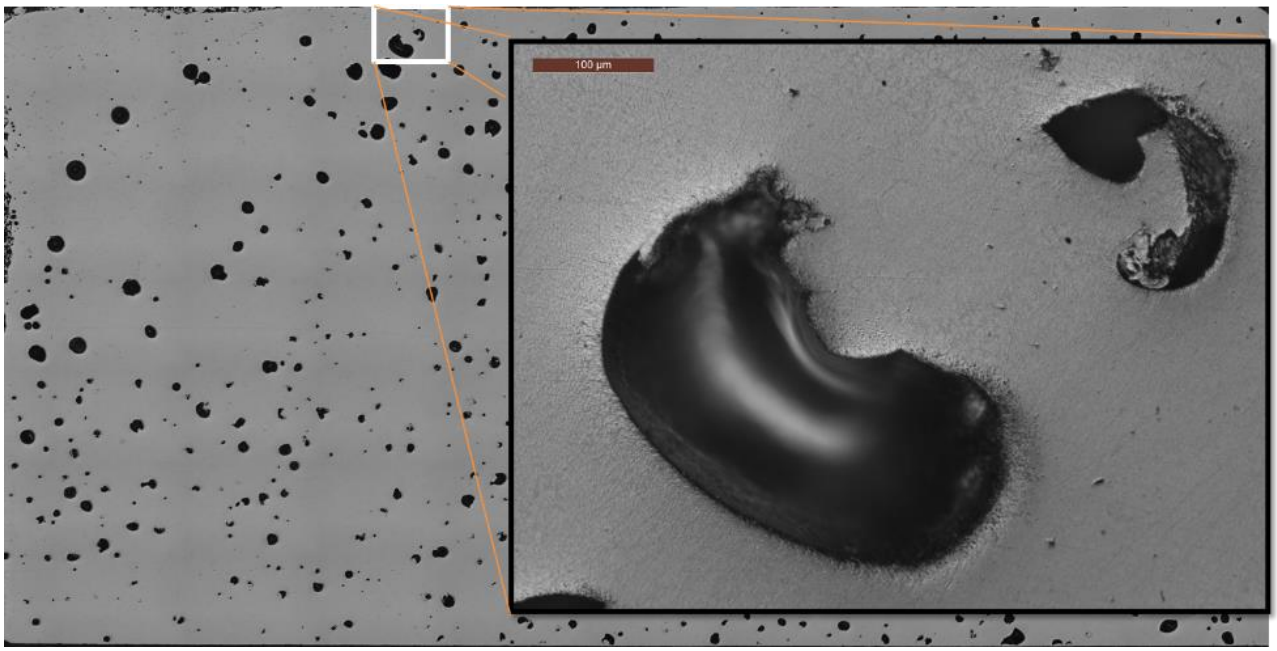


Figure 4.6 Example of Keyhole Porosity (XY)

The formation of keyhole porosity happens on the opposites spectrum of energy density. As described in section 2.3.2, keyhole form from instabilities created during keyhole-mode melting. As the energy density increases not only will the width of the weld pool grow, the depth will increase. To ensure that keyhole pores were formed in the characteristic cube a high energy density of 200 (J/m^3) was utilized. This resulted in a much larger weld pool widths and depth, while the hatch spacing is only 100 micrometers, the same size as the beam diameter. Accordingly, each raster of the laser would result in several rasters of the same layer being sequentially laser heated several times creating deep penetrating melt pools. Because of this continual over heating the characteristic cube is riddled with keyhole porosity throughout its bulk. Figure 4.6 shows a micrograph from the keyhole characteristic cube. The cube is saturated with oval shaped keyhole porosity because of the high energy input. The pores vary in size from 20 to over 100 microns in diameter.

While LOF and keyhole porosity depend primarily on the energy density, gas porosity morphology can be dependent several circumstances as discussed in section 2.3.3. The bulk melting parameters used in making the gas cube are the same parameters by which the REC samples were made, however the use of a pre-scanning technique was not used. Figure 4.7 displays a micrograph from the gas porosity characteristic cube. Small spherical pores are present throughout the entirety of the cube. These pores vary in size from sub micro to 20 microns in diameter. An investigation has been done to determine the

role the hydrogen concentration plays in the nucleation of gas pores and will be discussed in chapters 5 and 6. The implications of the solidification conditions on the hydrogen concentrations and weld pool interactions will determine whether gas porosity can nucleate. Whether by nucleation or by some other means the effects gas porosity will negatively impact density in the as built parts.

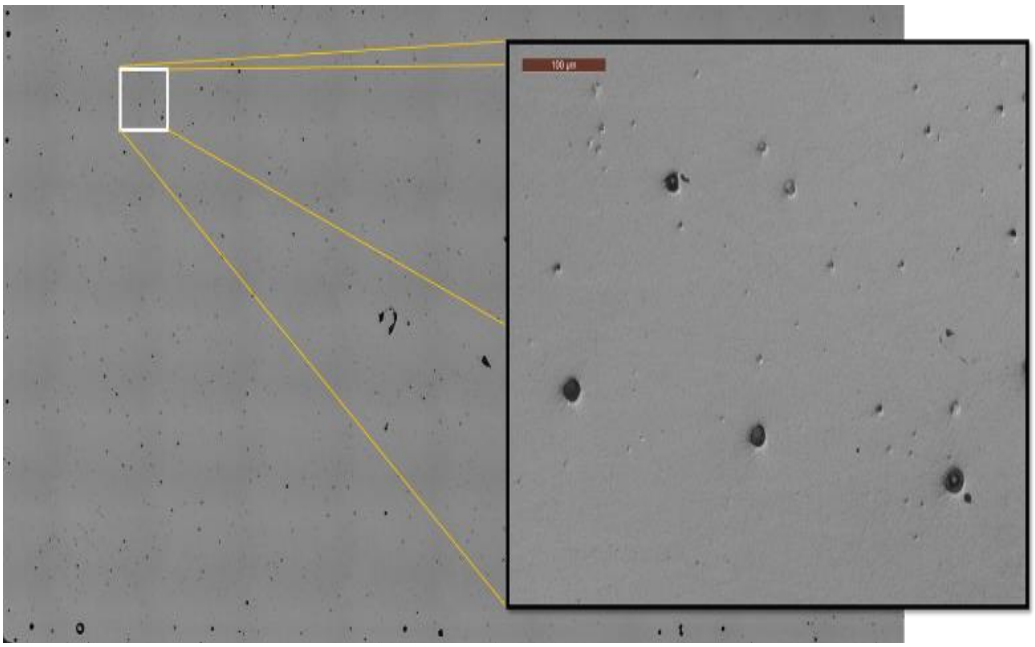


Figure 4.7 Gas Cube Micrograph Displaying small spherical Gas porosity

4.4 Hydrogen reduction technique

An investigation spanning two sets of builds created by two different L-PBF machines was performed to quantify the effects of pre-scanning as discussed in section 2.3.3. The following results consist of density measurements obtained by optical images of polished samples and with the use of a pycnometer. Figures 4.8 represent the REC samples made on the Concept Laser Xline 1000, REC 1 and 2 were built with the pre-scan parameters, and 3 and 4 without. Tables 4.4 display samples pycnometer measured density. The percent dense value is calculated as the measured density divided by the theoretical density of AlSi10Mg which is 2.67 g/cm^3. The pre-scanned REC samples (1,2) show an increase in density over the ones built without.

The micrographs were taken of polished sections of the REC samples. ImageJ was utilized to measure the optical density of the bulk material. The edges of the pictures were not included to ensure that only a measurement of the bulk density was calculated. Table 4.5 shows the results of the optically measured density for the rectangular cubes. The density increase between pre-scan and no pre-scan shown in the pycnometer samples is not seen in the optically measured stitched micrographs. This could be attributed to the fact that the optical density does not represent the entire volume but only an 2D areal density and that the resolution of the stitch image was not high enough to reveal micron size gas pores.

Table 4.4 Pycnometer Density measurements REC samples

Sample	Density (g/cm^3)	STD (g/cm^3)	% Dense
REC 1 Pre	2.6447	0.0008	99.052%
REC 2 Pre	2.6456	0.0007	99.086%
REC 3	2.6259	0.0004	98.348%
REC 4	2.6281	0.0004	98.431%

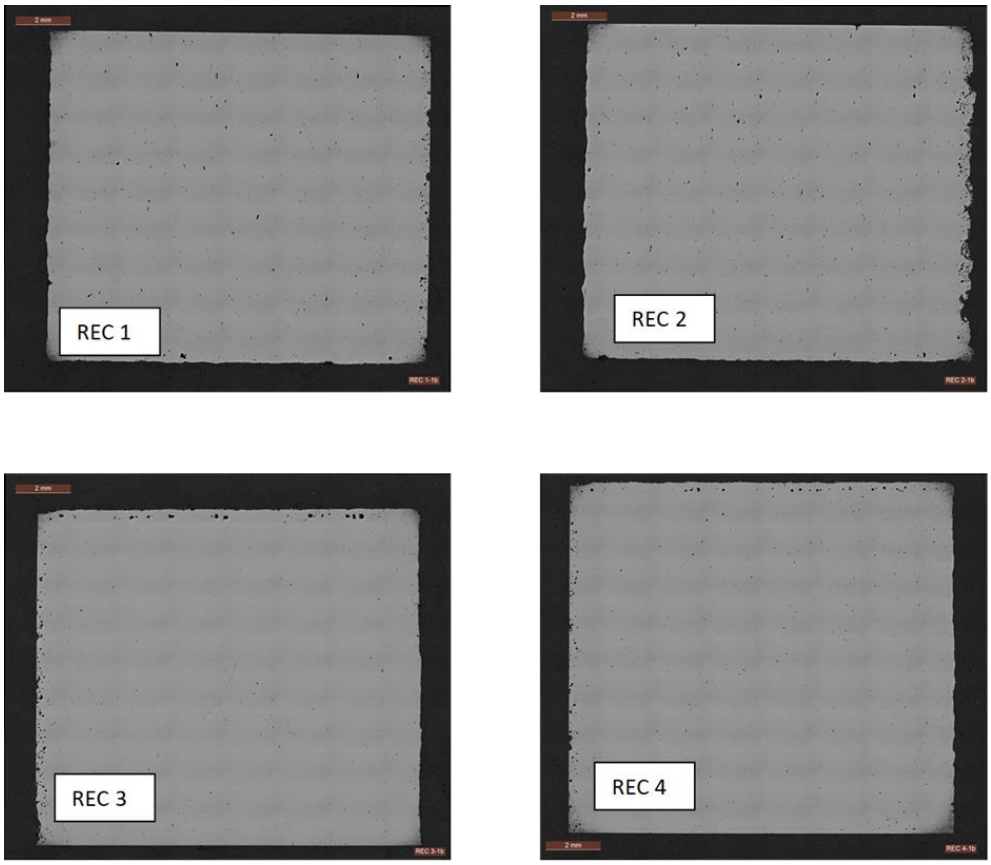


Figure 4.8 Micrographs of all REC samples. Samples 1 and 2 were created with the Pre-Scanning Technique

Table 4.5 Optically measured areal density REC samples

Sample	% Dense
REC 1 P	99.657 %
REC 2 P	99.6275 %
REC 3	99.607 %
REC 4	99.639 %

Because the stitched micrograph does not provide a fine enough resolution for investigation of pores on the same scales as the microstructure observed, a new technique was adopted. To resolve this issue, several high-resolution images were randomly taken of each REC sample. Image particle analysis was completed on each image and the resulting porosity count is represented in figures 4.9 and 4.10. Here instead of just a simple count of pores of a certain diameter, the count was divided by the total area of all nine pictures to give a count per square millimeter. Notice that in the range of 2-10 µm diameter pores the pre-scanned samples (REC 1 and 2) trend lower than REC 3 and 4. This is especially apparent in the XY micrographs were the number of occurrences per square mm for samples 1 and 2 drop to almost none as opposed to 3 and 4 which trends around 20. This trend was not apparent in the XZ micrographs and is possibly a result of the where the sample was sectioned.

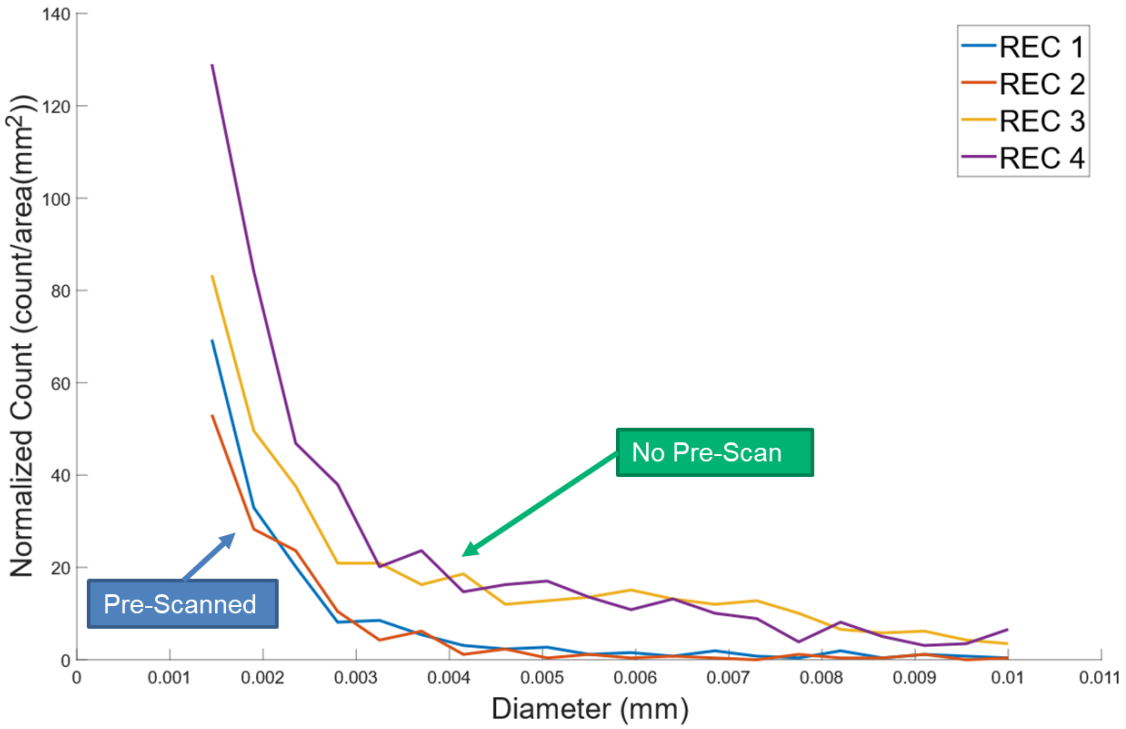


Figure 4.9 Areal Count of Micron Size Pores in the XY micrographs of all REC samples

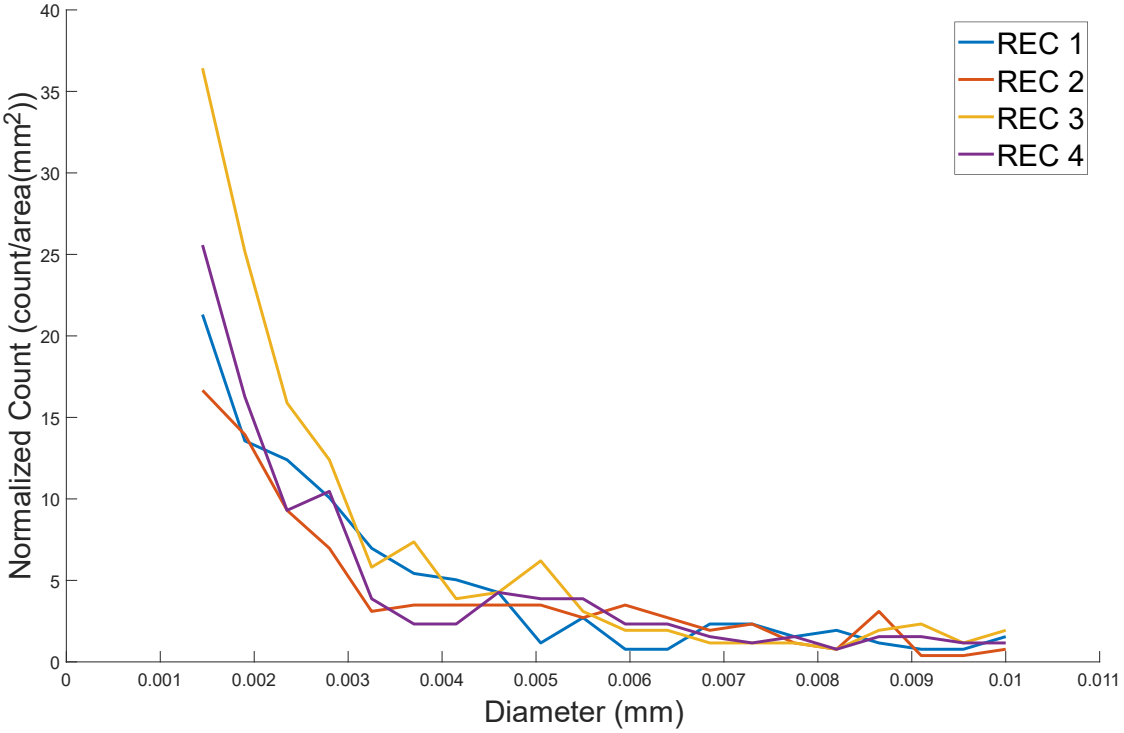


Figure 4.10 Areal count of micron size pores in XZ REC micrographs

The samples produce by the SLM machine show a slight difference between densities. Figure 4.11 represent the rectangular cubes manufactured on the SLM system. 51AP and 51BP were built with the pre-scan technique, and 51A and 51B without. Several high-resolution images were taken of cubes 51B and 51BP to analyze differences in pore size on a micron level. The resulting pore count per millimeter squared can be seen in figure 4.12 and is the same analysis that was completed for the REC samples. The 51A and 51AP samples show no trend as seen in the REC samples, however the pre-scanned sample 51BP shows a lower count between pore diameters of 3 to 5 micrometers. This is a similar trend that was seen in the REC samples. However, the 51B sample trends lower than the REC 3 and 4 samples by almost half. Rationalization as to why this difference is occurring could stem from the hydrogen content in the powder that was used by the different machines.

Table 4.6 represents the 51 samples pycnometer measured density. The percent dense value is calculated as the measured density divided by the theoretical density of AlSi10Mg which is 2.67 g/cm^3. The samples produce by the SLM machine do not show an increase in density due to pre-scan. This is attributed to a unique phenomenon were large spherical pores were induced due to the software control of the stipe pattern being utilized. Therefore, the density values from all four samples trend lower than those of the REC samples. No noticeable difference was observed in the optically measured density as well. Table 4.7 shows these results and confirms no noticeable increase in density due to the pre-scanning technique.

Sections from REC and 51 was sent off to test the total amount of hydrogen by inert gas fusion. Samples REC 1 and REC 2 both showed a marked reduction in overall hydrogen content versus the samples manufactured without the pre-scan. The samples sent off for hydrogen testing do however shows a drop in concentration with respect to sample 51A. The value of hydrogen measured is reduced between samples 51A and 51AP but remain constant for 51B and 51BP. This inconsistency could stem from the differing parameters used on the SLM samples as opposed to the Concept laser samples. Table 4.8 shows the results from the inert gas fusion testing. This shows a significant drop from the measured content of the powder samples. However, because of the error involved with the inert gas fusion method no assumptions can be made in the overall effectiveness of reducing hydrogen content through the pre-scanning technique. These results do provide a scale of the final hydrogen content trapped in both the gas pores and in the aluminum matrix. These values are also an order of magnitude higher than the solubility of hydrogen at the melting temperature 0.625 (ppm)[18].

Table 4.6 Pycnometer readings of all samples produced on the SLM 280 System.

Sample	Density (g/cm^3)	STD (g/cm^3)	% Dense
51A	2.6383	0.0003	98.719%
51AP	2.6365	0.0003	98.745%
51B	2.6314	0.0002	98.554%
51BP	2.6396	0.0004	98.861%

Table 4.7 Optically measured Density

Sample	% Dense
51A	99.56%
51AP	99.01%
51B	99.79%
51BP	99.90%

Table 4.8 Hydrogen concentrations from both REC and 51 samples

Sample Identification:	Hydrogen ppm	+/- PPM
51A-2B	8	2
51AP-2B	6	2
51B-2B	6	2
51BP-2B	6	2
REC 1 AR	4	2
REC 2 AR	5	2
REC 3 Gas	8	2
REC 4 Gas	7	2

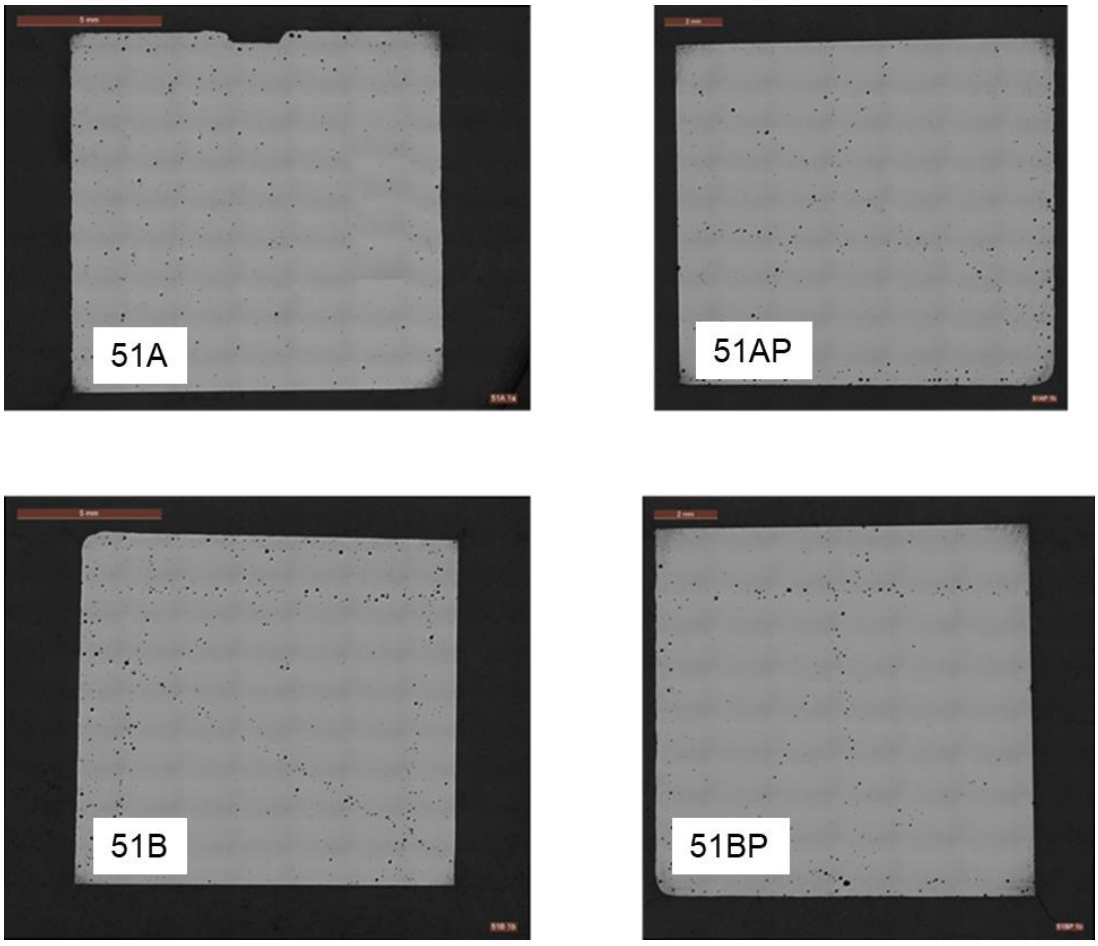


Figure 4.11 Stitched micrographs of samples produced on the SLM 280 Samples 51AP and 51BP were created using the Pre-Scanning Technique

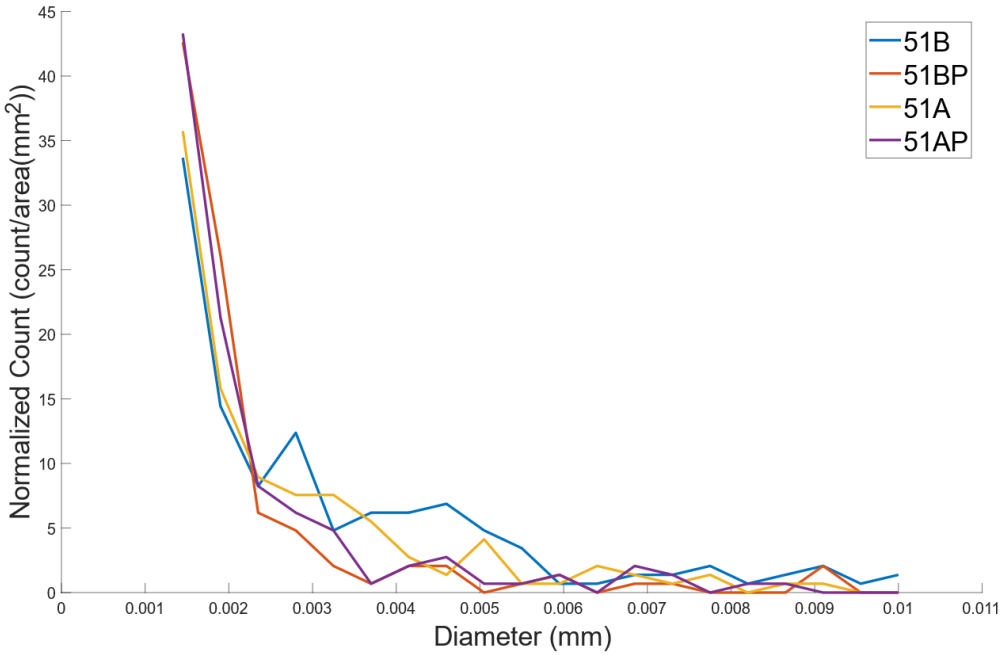


Figure 4.12 Areal Density of the XY micrographs of all samples produced on the SLM 280

4.5 Gas pore mechanisms

The understanding of gas pore morphology during the L-PBF has not been thoroughly research at this point. For a gas pore to form, a nucleation event must take place, or the pore already exist. Figure 4.13 shows examples of these two mechanisms and the different circumstances that may generate gas bubbles in the melt pool. This section will discuss the nucleation events and seek to understand the hydrogen concentrations at the solidification front. In sections 4.5.1-4.5.5 hydrogen pore nucleation is explained and the evolution of gas concentration in solidifying metal is discussed. Section 4.5.2 will discuss gas pores found in the weld pools of AlSi10Mg and seek to give reasoning to their existence.

4.5.1 Hydrogen pore nucleation.

Nucleation of a gas pore is only possible when the liquid-gas interface energy can be surmounted by the supersaturation in the liquid metal. However, Campbell et al and other authors have proposed that homogenous nucleation of gas pores is not possible[36], [37]. This is due to the relationship of the pressure inside the nucleated gas pore to the liquid pressure surrounding it. As discussed in section 2.3.3, the pore pressure can be represented as.

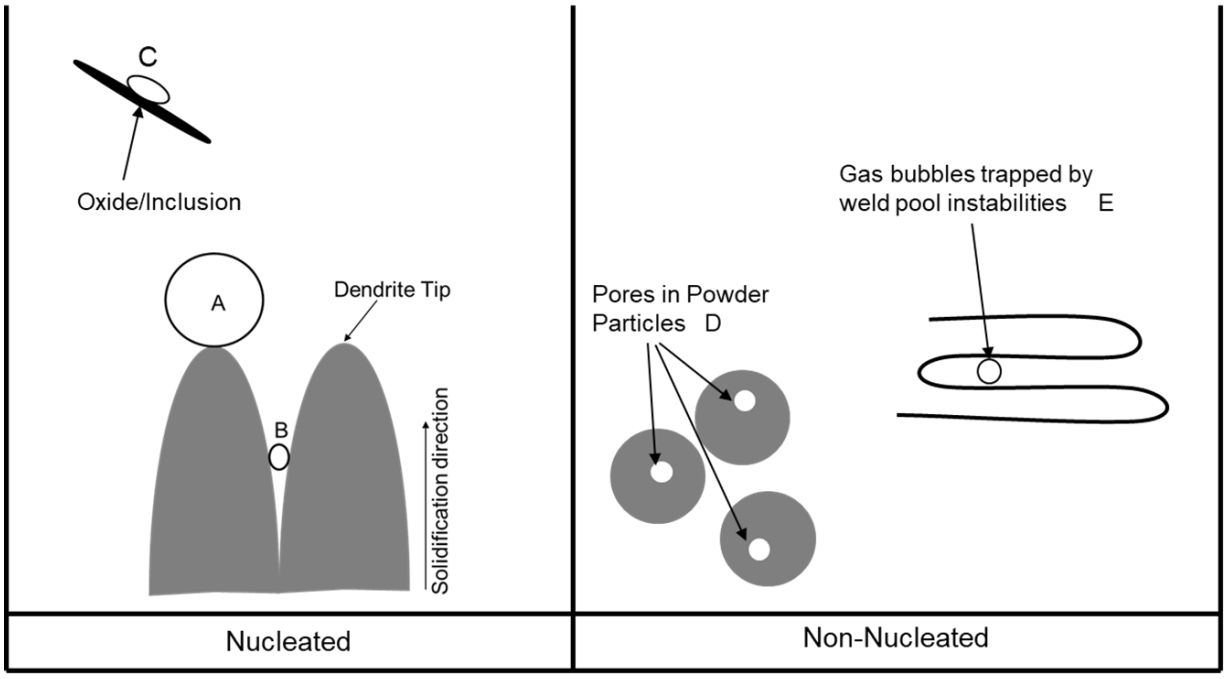


Figure 4.13 Different mechanisms for gas bubble generation within L-PBF process.

$$P_p = P_l + \frac{2\gamma_{lp}}{R_p} \tag{7}$$

Where γ_{lp} is the interfacial energy, R_p is the nucleating pore radius and P_l is the liquid pressure. If pores nucleate on a nanometer scale the pressure difference across the gas liquid interface would need to be in the GigaPascal range. Therefore, it is concluded that nucleation happens heterogeneously and must be aided by some type of substrate. For the cellular dendritic solidification observed in L-PBF of AlSi10Mg alloys, the question then becomes does nucleation occur at the dendrite tip, somewhere besides the solidification front, or between the dendrites? A representation of two of these nucleation sites is shown in figure 4.14 with respect to the solidification front. The next two sections will discuss the supersaturation of hydrogen at these specific locations and rationalize the propensity of a pore to nucleate at two different regions of the weld pool. It is important to understand the scale of gas pores found in L-PBF relative to the scale of the microstructure. If a pore nucleated in-front of the solidifying dendrite tip (pore A) it could potentially grow to a diameter great than that of the dendrite, however if the pore nucleates between the dendrites (pore B) it will retain the same scale as the primary dendrite arm spacing(PDAS).

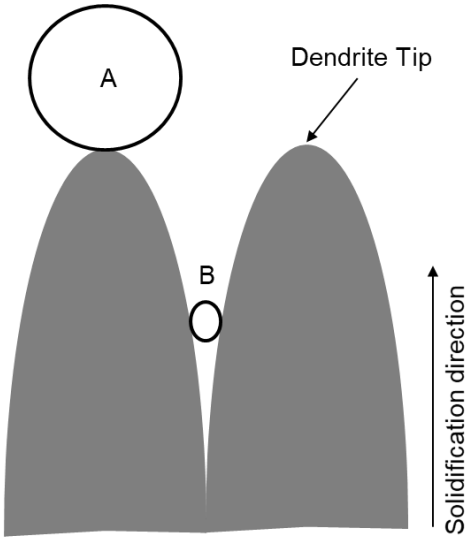


Figure 4.14 Gas bubble nucleation at the solidification front

4.5.2 Concentration of hydrogen around a dendrite tip due to growth velocity

Understanding how the concentration of hydrogen changes during solidification requires knowledge of both the temperature and solute fields. The presence of cellular dendritic growth throughout the weld pools is common in L-PBF as discussed in section 2.4. If observed locally the dendrite growth can be thought of as directional solidification and the shape of the dendrite as a paraboloid. Figure 4.15 is a representation of this dendritic growth. As the dendrite grows in direction z at a certain velocity R (solidification front velocity), the flow of the liquid around the tip creates thermal and solutal boundary layers. Although the dendrite is growing into the liquid it is common approach to think of the liquid flowing around the tip.

The 3D temperature distribution around a parabolic dendrite tip can be calculated as[37]

$$\theta_l = \frac{E_1(Pe\xi^2)}{E_1(Pe)} \tag{8}$$

Where the dimensionless temperature is defined as $\theta_l = \frac{T_l - T_o}{T_f - T_o}$, Pe is the Peclet number, ξ is the paraboloidal coordinates around the dendrite tip and E_1 is the exponential integral equal to

$$E_1(x) = \int_x^\infty \frac{e^{-s}}{s} ds \tag{9}$$

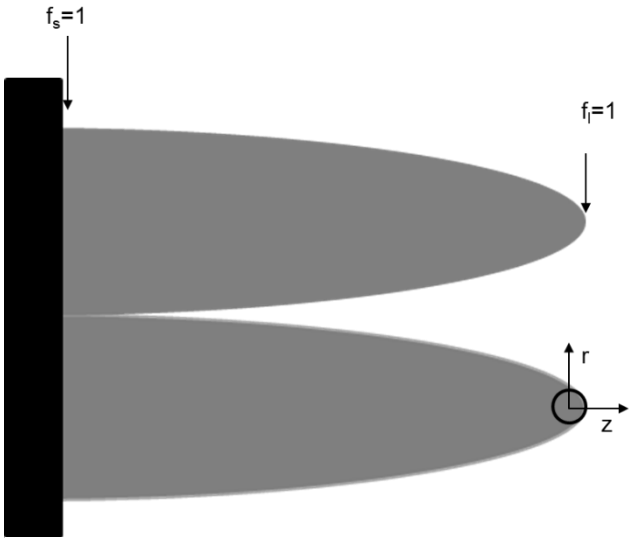


Figure 4.15 Solidifying dendrites

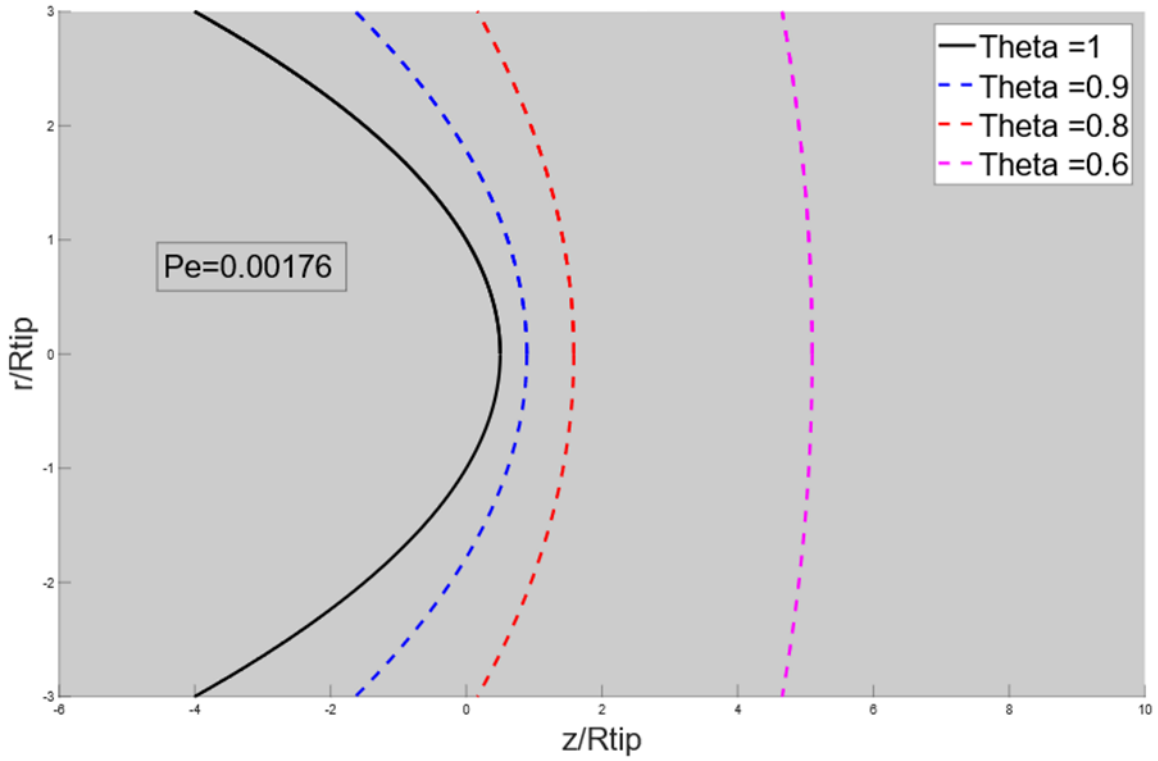


Figure 4.16 Dimensionless Temperature profile around the dendrite tip

To calculate the Peclet number the solidification velocity, tip radius, and thermal diffusivity must be known as $Pe = \frac{Rr_{tip}}{2\alpha_l}$. In this case these three variables were selected as R=0.5 m/s, r_{tip}=500 nm, and α_l=7.1x10^{-5} m^2/s. The corresponding dimensionless temperature distribution can be seen in figure 4.16. Similarly, a solute field for hydrogen concentration was created based up equation 8, however Pe is based upon hydrogen's diffusion constant and is a representation of mass transport instead of heat flow. Therefore, Pe_C is the measurement of advection and diffusion and is equal to.

$$Pe_c = \frac{Rr_{tip}}{D_H} \tag{10}$$

Where D_H is the diffusion constant of hydrogen and equal to 2.49x10^{-7} m^2/s. The supersaturation of this solute field at the boundary condition at the liquid solid interface is known as the Ivantsov function (equation 11)[45].

$$\varphi = \frac{C_l^* - C_o}{C_l^*(1 - k_o)} = Pe_C \exp(Pe_C)\, E_1(Pe_C) \tag{11}$$

Where C_l^* is the concentration of at the solid liquid interface, C_o is the initial concentration in the liquid, and k_o is the partition coefficient of hydrogen. Because Pe_c is a constant and known the concentration at the solid liquid interface can be calculated by equation 12.

$$C_l^* = \frac{C_o}{(1 - \varphi(1 - k_o))} \tag{12}$$

Therefore, by knowing the initial concentration, the concentration at the solid liquid interface, and the solute field, the concentration around the dendrite tip can be calculated. The Pe_c of the hydrogen is dependent on R^*r_{tip} and during L-PBF the dendrite tip radius is dependent on the local solidification conditions namely R, the solutal Pe_C (in this case silicon), and G (thermal gradient)[46].

In this case R^*r_{tip} parameter has been chosen at two different points in the weld pool. At the base of the weld pool the thermal gradients are the highest and the solidification front velocity is the slowest, and at the tail the thermal gradients are the lowest and velocity is the fastest. Estimation of the R^*r_{tip} parameter was done with a model developed by Plotkowski et al but has been adapted for the current alloy[46]. The resulting concentrations fields for the different points in the weld pool are

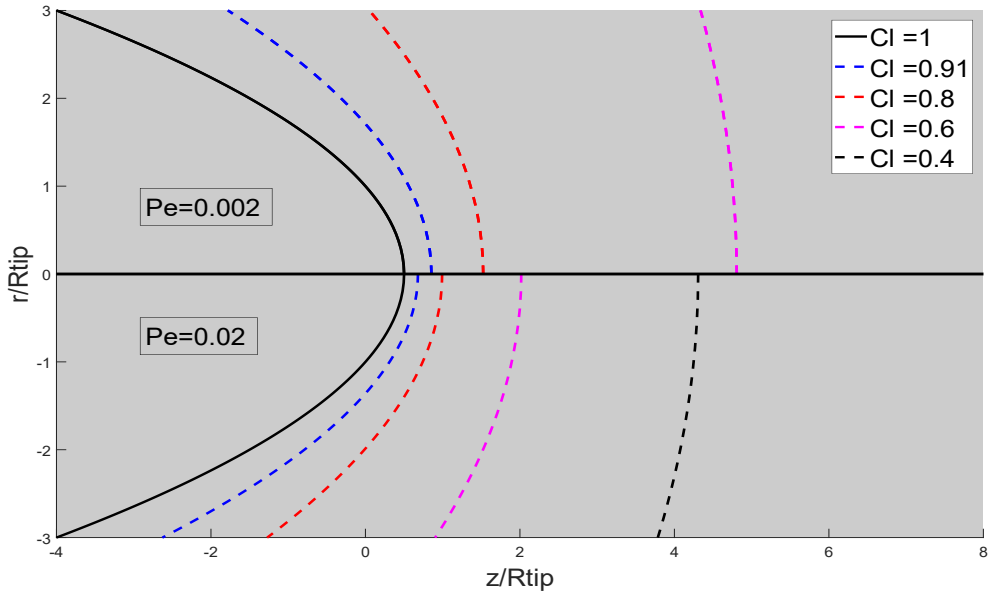


Figure 4.17 Hydrogen Concentration fields around the dendrite tip at two different Peclet numbers

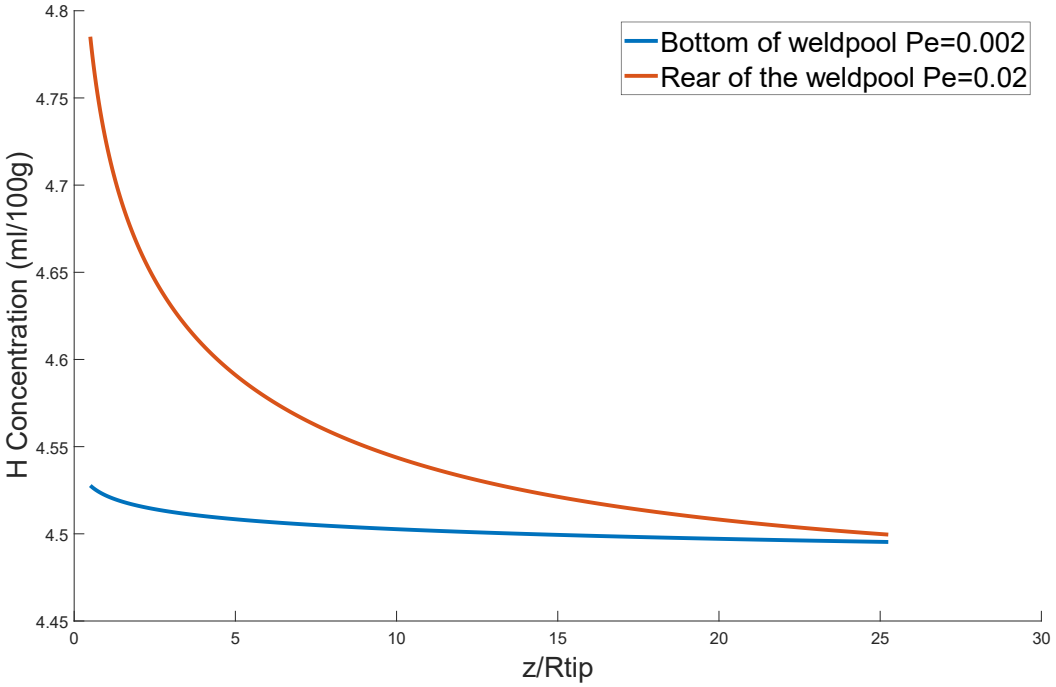


Figure 4.18 Hydrogen supersaturation in the liquid in-front of the solidifying dendrite tip

plotted in figure 4.17, and the supersaturations are seen in figure 4.18 for an initial concentration of 4.48 (ml H/100g Al)

This increase in saturation is due to the solutal fields in front of the dendrite tip and does not consider the change in concentration due to solidification. The saturation at the liquid-solid interface is higher for dendrites solidifying at the rear of the weld pool. This understanding would suggest that the propensity of a hydrogen pore to nucleate in-front of the solidification front is greater at the rear of the weld pool where solidification velocities are higher.

4.5.3 Concentration of hydrogen due to solidification.

The concentration of hydrogen also increases due to the liquid volume fraction shrinking during solidification. To determine the rate of shrinkage a Scheil diagram was generated with Thermocalc software for the alloy system AlSi10. This diagram plots the fraction solid as a function of temperature and is shown in figure 4.19. Notice that the aluminum phase is almost completely solidified at gs=.2,

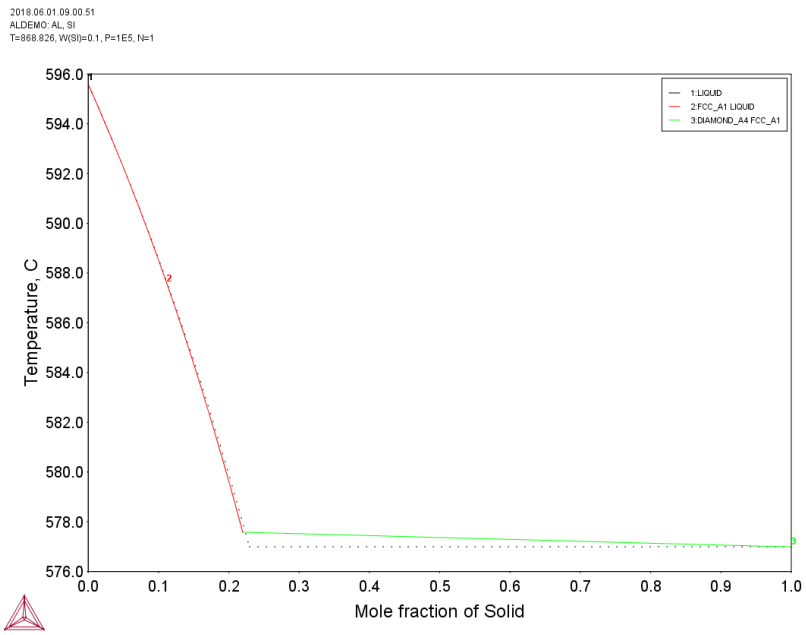


Figure 4.19 Scheil diagram for the AlSi10 alloy

and that the temperature change during the silicon solidification is very small. After that point a silicon rich eutectic is predicted to form between the cellular dendrites. For this reason, only a gs range of 0-.22 was used in the calculation of the concentration of Hydrogen in the liquid at various solid fraction. A simple Concentration balance for any point along the gs line can be calculated as

$$Co = g_s C_{gs} + g_l C_{gl} \tag{13}$$

Where gs and gl are the solid faction and liquid fraction and C_{gs} is the concentration of the concentration of the gas in the solid and C_{gl} is the concentration of the gas in the liquid. However, C_{gs} can be calculated with the use of the partition coefficient of hydrogen in solid aluminum which in this case was set as k_o =.07 and C_{gs}=.07*C_{gl}. Therefore, the Concentration in the liquid at any solid fraction can be calculated as

$$C_{gl} = \frac{Co}{(k_o g_s + (1 - g_s))} \tag{14}$$

Figure 4.20 displays how C_{gl} increases as a function of g_s and by the time the aluminum alpha phase has formed completely the concentration has risen 30 percent.

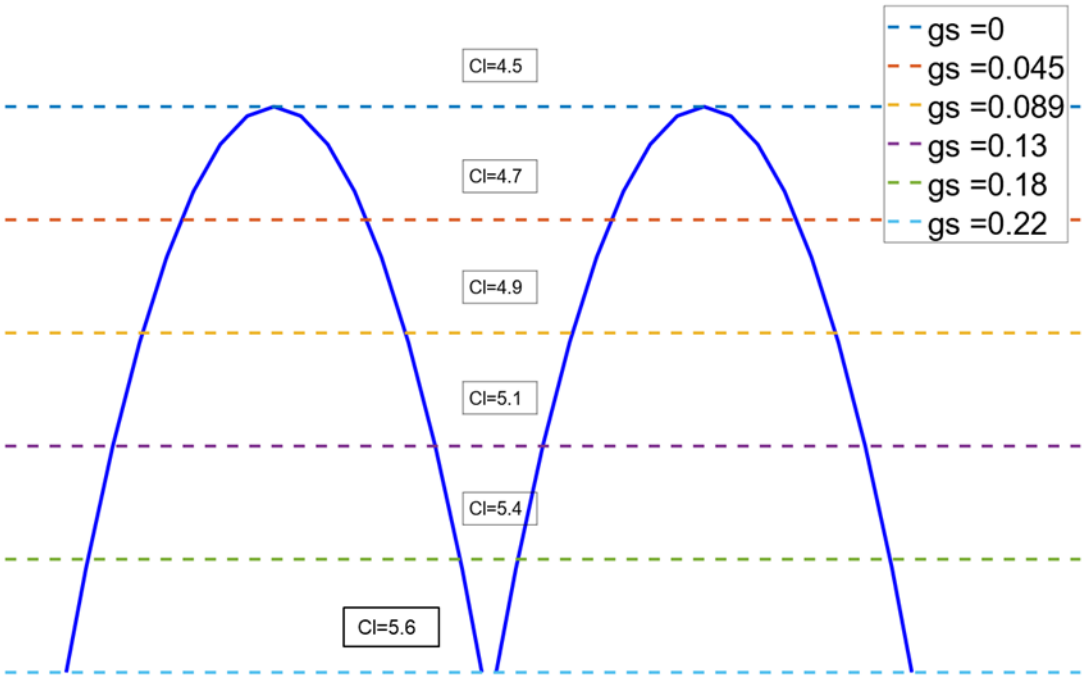


Figure 4.20 Increasing Hydrogen concentration between the Dendrite Tips

The effects of increased concentration due decrease in liquid fraction where not coupled with those of the solute field as discussed in 4.5.2. If coupled the effects of the solute fields based upon the Peclet number would either increase or decrease the supersaturation values at the inter dendritic solid liquid interfaces. Because the pore must nucleate heterogeneously the value of supersaturation at the solid liquid interface will determine at which position nucleation will occur.

4.5.4 Hydrogen concentration equilibrium

To compare the measured final concentrations in the builds from section 4.4 to the concentrations necessary to homogenously nucleate a gas bubble, Sievert's Law was employed (equation 15). This law states that the partial pressure of a gas bubble in a liquid reservoir is proportional to the concentration of the gas in solute at the solid liquid interface.

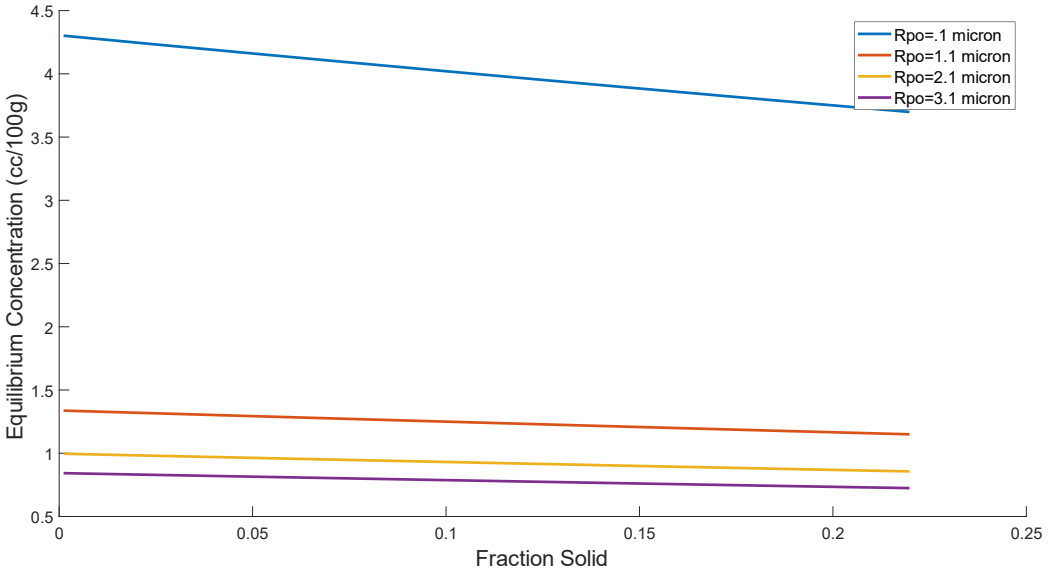
$$C_{gl}^{eq} = \frac{Ke}{f}\left(\frac{P_p}{P_{atm}}\right)^{1/2} \tag{15}$$

In equation 14 Ke is the equilibrium coefficient based upon temperature, f is the activity coefficient of the gas, P_P is the partial pressure of the gas inside the bubble, and P_{atm} is the atmospheric pressure. To calculate the partial pressure of the gas bubble the Young-Laplace equation (equation 7) was utilized and based upon the initial radius of a nucleated pore. However, the shrinkage pressure of the inter-dendritic liquid must be known and can be calculated as equation 16[47].

$$P_l = P_{atm} - \left[\frac{180}{\lambda}\frac{v_t \beta \mu}{G}\int_{T_x}^{T_l}\left(\frac{g_s(T)^2}{1-g_s(T)^2}\right)dT\right] \quad (16)$$

Where λ is the primary dendrite arm spacing, v_t is the isotherm velocity, G is the thermal gradient, β is the solidification shrinkage factor, μ is the liquid dynamic viscosity, and g_s is the fraction solid as a function of temperature. The resulting hydrogen concentration equilibriums are plotted as a function of both initial pore size and fraction solid in figure 4.21.

As the initial pore size decreases to 100 nm the equilibrium concentration increases in the liquid. This illustrates the influence of the shrinkage pressure/microsegregation (the slope of the line) and the pore radius at the same time. If the equilibrium concentrations of hydrogen are overlaid over the calculated concentration in the liquid (figure 4.22) from section 4.5.4 it is evident that the lowest measured concentration in the builds from section 4.4 is larger than the amount required to homogenously nucleate a gas bubble in between dendrites



. Figure 4.21 Equilibrium Hydrogen Concentration as a function of fraction solid and initial pore radius

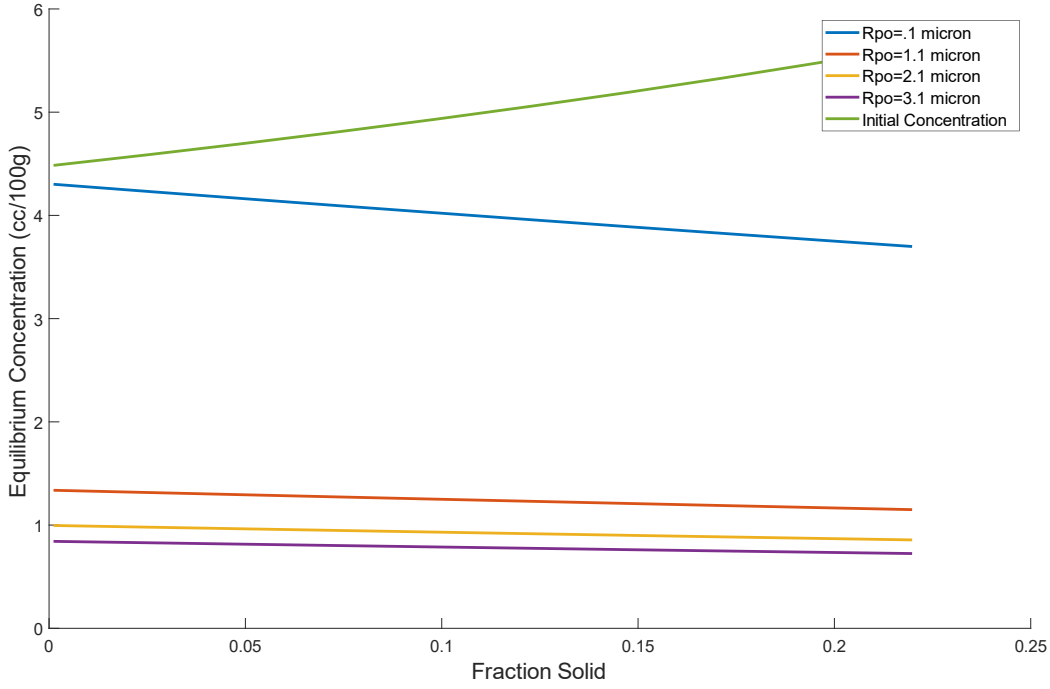


Figure 4.22 Equilibrium and inter-dendritic liquid Concentrations compared.

4.5.5 Sources of gas porosity

As discussed in section 4.5.1 homogenous nucleation is not possible for gas porosity and requires a substrate to occur. To understand the morphology of gas pores seen in L-PBF process micrographs were taken of etched samples of AlSi10Mg. Figures 4.23 and 4.24 show xz micrographs of the gas cube from section 4.3. It is evident that many of the gas pores are much larger than the surrounding microstructure within figure 4.24. This would lend itself to the theory that the pores either nucleated at the tip of the solidifying dendrite or nucleated on something besides the solidifying microstructure. Oxides or inclusions carried by currents within the weld pool will have concentration fields and pores could nucleate heterogeneously on them. It could be possible that the pore did not nucleate and was originally in the powder and upon melting was unable to escape the weld pool. Instabilities in the weld pool could potential captured gas from the environment and the resulting bubble was entrapped by solidification. The last two mechanisms would be considered non-nucleation events and would explain the larger diameter porosities seen in figure 4.23.

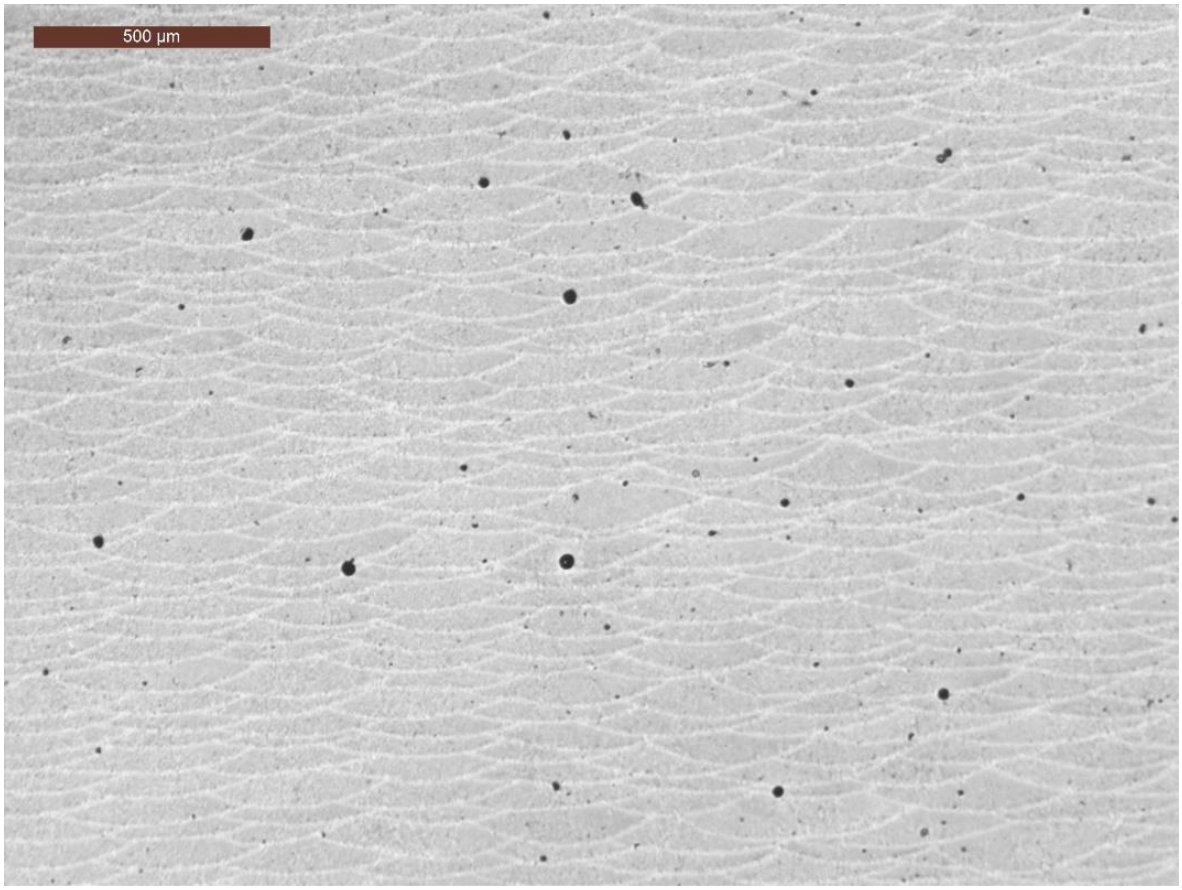


Figure 4.23 Etched Micrograph of Gas pore cube from chapter 4 (XZ direction)

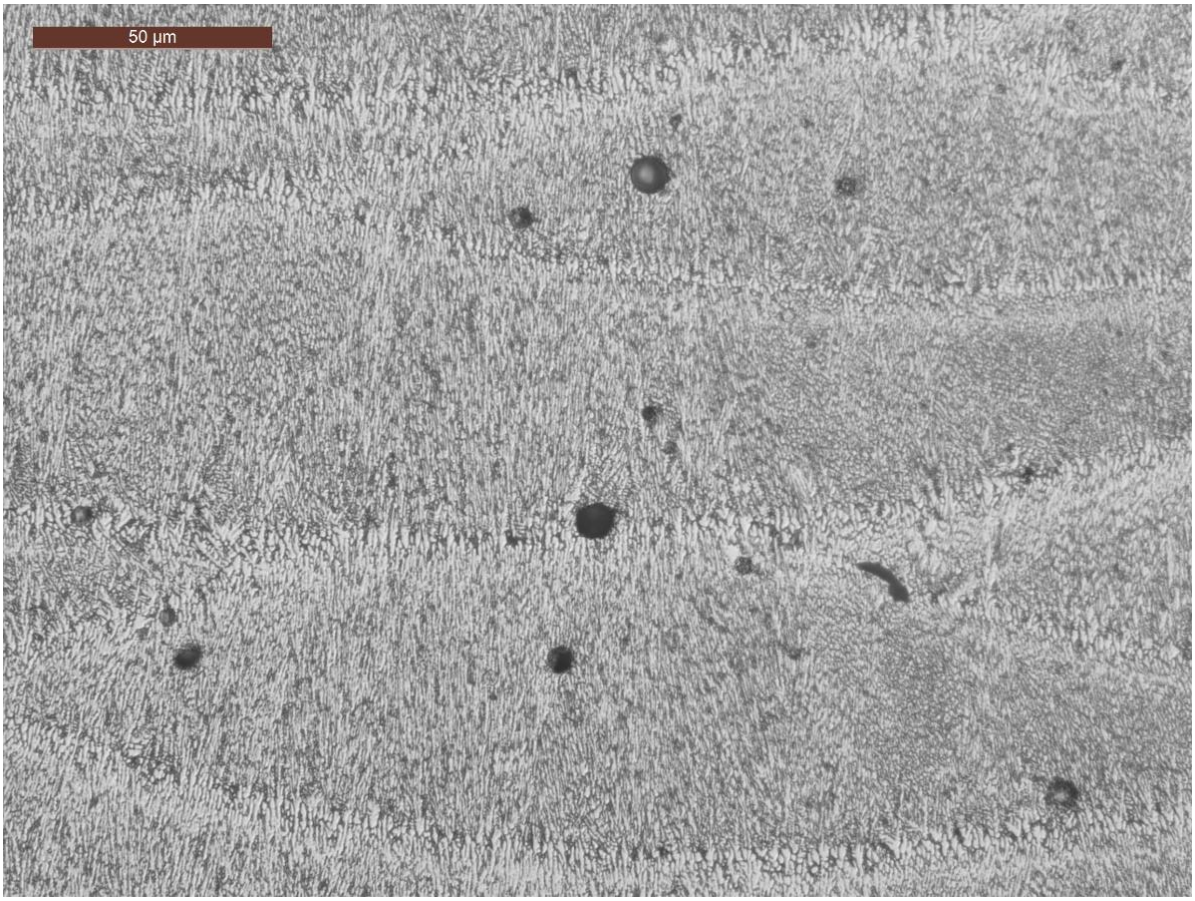


Figure 4.24 Higher Resolution image of figure 6.11 displaying gas pores of various sizes.

Chapter 5 Future work

At the conclusion of this body of work several avenues of future work are presented. Currently work is being done at Argon National Labs for in-situ x-ray CT scanning of solidifying weld pools. This process would allow for nucleation events to be observed during different melting parameters. Therefore, relationships could be linked from input parameters to the solidification parameters that control the nucleation rates of hydrogen gas pores. With this understanding further work would entail modeling the solidification parameters of complex geometry parts and link those back to the nucleation rates observed during the x-ray CT scanning. These steps will lay the groundwork for the modeling of hydrogen concentration and pore nucleation based upon the work performed in this thesis.

Another area would be a thorough investigation of the hydrogen reduction methods. Methods to reduce hydrogen content in the powder to levels consistent to casting and welding process will decrease the propensity to nucleate pores in the L-PBF process. Although this process seems more tenuous, less complex solutions are beginning to emerge. A simple addition of a descant packet has been shown to reduce humidity levels found in new powder.

In retrospect further analysis of the pre-scanned powder samples could have given evidence of the effects of the reduction of hydrogen from those measured in the new powder samples. Comparisons could have also been drawn between the final measured hydrogen concentration to those in the pre-scanned powder. Another characterization of the hydrogen content that could have been performed is the fracturing technique. Samples are fractured in a vacuum chamber and the gases released are measured by a mass spectrometer. These values could have been compared to the overall contents measured by inert gas fusion and relationships to the supersaturation in the aluminum matrix could be calculated.

Chapter 6 Summary and conclusions.

Defects in as-built parts can negatively impact properties and confidence placed in L-PBF AlSi10Mg parts. Three specific pore defects were analyzed and the morphology, shape, and size was discussed. Lack-of-fusion and keyhole porosity were shown to stem from too little or too much input energy respectively. Gas pores morphology was shown to stem from several different mechanisms, however in the case of aluminum alloys, the contamination of hydrogen can increase the nucleation of gas pores. The sources of the hydrogen are generally assumed to come from primarily moisture on the surface of the powder and hydrogen trap in solution with the aluminum. A pre-scanning technique was utilized in two different L-PBF systems to quantify the reduction of hydrogen content in as built parts. The samples made by the Concept Laser system showed a marked reduction of hydrogen in the pre-scanned samples and resulted in an increase in density. The results of samples made in the SLM 280 were skewed by an issue with the software that controlled the scan strategy which induced lines of keyhole porosities throughout all four parts. The pre-scanned powder was also analyzed and displayed an increase porosity within the powder particles when compared to “new” powder.

Finally, the increase of hydrogen concentrations at the solidification front was simulated for two uncoupled conditions. The first is the supersaturation at the growing dendrite tip was calculated by the Ivantsov solution which is dependent on the growth velocity and tip radius. This supersaturation was estimated for two positions in the weld pool and it was found that larger tip radii leads to a lower supersaturation at the solid-liquid interface compared to the high solidification velocities at the tail. The second condition is the increase in concentration between solidifying dendrites due to hydrogen rejection from the solid to the liquid aluminum. The increase of concentration is compared to the relative equilibrium concentration due to Sievert’s Law for varying nucleation pore radius. It was shown that down to a nucleation radius of 100 nm, the final concentration measured from the builds in chapter five were enough to homogenously nucleate hydrogen gas pores. Therefore, the overall issue concerning hydrogen pore nucleation reverts to a more thorough understanding of the nucleation rates based upon the solidification parameters.

Bibliography

[1] W. J. Sames, F. A. List, S. Pannala, R. R. Dehoff, and S. S. Babu, “The metallurgy and processing science of metal additive manufacturing,” *Int. Mater. Rev.*, vol. 6608, no. March, pp. 1–46, 2016.

[2] W. E. Frazier, “Metal additive manufacturing: A review,” *J. Mater. Eng. Perform.*, vol. 23, no. 6, pp. 1917–1928, 2014.

[3] L. E. Murr *et al.*, “Fabrication of metal and alloy components by additive manufacturing: Examples of 3D materials science,” *J. Mater. Res. Technol.*, vol. 1, no. 1, pp. 42–54, 2012.

[4] M. Tang, P. C. Pistorius, and J. L. Beuth, “Prediction of lack-of-fusion porosity for powder bed fusion,” *Addit. Manuf.*, vol. 14, pp. 39–48, 2017.

[5] T. Kimura and T. Nakamoto, “Microstructures and mechanical properties of A356 (AlSi7Mg0.3) aluminum alloy fabricated by selective laser melting,” *Mater. Des.*, vol. 89, pp. 1294–1301, 2016.

[6] H. Gong, K. Rafi, H. Gu, T. Starr, and B. Stucker, “Analysis of defect generation in Ti-6Al-4V parts made using powder bed fusion additive manufacturing processes,” *Addit. Manuf.*, vol. 1, pp. 87–98, 2014.

[7] A. Plotkowski, M. M. Kirka, and S. S. Babu, “Verification and validation of a rapid heat transfer calculation methodology for transient melt pool solidification conditions in powder bed metal additive manufacturing,” *Addit. Manuf.*, vol. 18, pp. 256–268, 2017.

[8] L. Thijs, K. Kempen, J. P. Kruth, and J. Van Humbeeck, “Fine-structured aluminium products with controllable texture by selective laser melting of pre-alloyed AlSi10Mg powder,” *Acta Mater.*, vol. 61, no. 5, pp. 1809–1819, 2013.

[9] L. Thijs, F. Verhaeghe, T. Craeghs, J. Van Humbeeck, and J. P. Kruth, “A study of the microstructural evolution during selective laser melting of Ti-6Al-4V,” *Acta Mater.*, vol. 58, no. 9, pp. 3303–3312, 2010.

[10] I. Yadroitsev and I. Yadroitsava, “Evaluation of residual stress in stainless steel 316L and Ti6Al4V samples produced by selective laser melting,” *Virtual Phys. Prototyp.*, vol. 10, no. 2, pp. 67–76, 2015.

[11] J.-P. Kruth, J. Deckers, E. Yasa, and R. Wauthlé, “Assessing and comparing influencing factors of residual stresses in selective laser melting using a novel analysis method,” *Proc. Inst. Mech. Eng. Part B J. Eng. Manuf.*, vol. 226, no. 6, pp. 980–991, 2012.

[12] E. Louvis, P. Fox, and C. J. Sutcliffe, “Selective laser melting of aluminium components,” *J. Mater. Process. Technol.*, vol. 211, no. 2, pp. 275–284, 2011.

[13] A. Ahmed, W. M. S., R. A. A., K. K., Q. Bakhsh, and D. Ali, “Effects of Selective Laser Melting Parameters on Relative Density of AlSi10Mg,” *Int. J. Eng. Technol.*, vol. 8, no. 6, pp. 2552–2557, 2016.

[14] E. Brandl, U. Heckenberger, V. Holzinger, and D. Buchbinder, “Additive manufactured AlSi10Mg samples using Selective Laser Melting (SLM): Microstructure, high cycle fatigue, and fracture behavior,” *Mater. Des.*, vol. 34, pp. 159–169, 2012.

[15] N. Read, W. Wang, K. Essa, and M. M. Attallah, “Selective laser melting of AlSi10Mg alloy: Process optimisation and mechanical properties development,” *Mater. Des.*, vol. 65, pp. 417–424, 2015.

[16] E. O. Olakanmi, R. F. Cochrane, and K. W. Dalgarno, “A review on selective laser sintering/melting

(SLS/SLM) of aluminium alloy powders: Processing, microstructure, and properties," *Prog. Mater. Sci.*, vol. 74, pp. 401–477, 2015.

[17] E. O. Olakanmi, "Selective laser sintering/melting (SLS/SLM) of pure Al, Al-Mg, and Al-Si powders: Effect of processing conditions and powder properties," *J. Mater. Process. Technol.*, vol. 213, no. 8, pp. 1387–1405, 2013.

[18] C. Weingarten, D. Buchbinder, N. Pirch, W. Meiners, K. Wissenbach, and R. Poprawe, "Formation and reduction of hydrogen porosity during selective laser melting of AlSi10Mg," *J. Mater. Process. Technol.*, vol. 221, pp. 112–120, 2015.

[19] D. Buchbinder, H. Schleifenbaum, S. Heidrich, W. Meiners, and J. Bültmann, "High power Selective Laser Melting (HP SLM) of aluminum parts," *Phys. Procedia*, vol. 12, no. PART 1, pp. 271–278, 2011.

[20] A. Kearney, *ASM handbook, vol. 2*. Materials Park, OH: ASM International, 1990.

[21] J. Campbell, *Castings, 2nd ed.* Butterworth-Heinemann, Oxford, 2003.

[22] B. Zhang, Y. Li, and Q. Bai, "Defect Formation Mechanisms in Selective Laser Melting: A Review," *Chinese J. Mech. Eng.*, vol. 30, no. 3, pp. 515–527, 2017.

[23] N. Saresh, M. G. Pillai, and J. Mathew, "Investigations into the effects of electron beam welding on thick Ti-6Al-4V titanium alloy," *J. Mater. Process. Technol.*, vol. 192–193, pp. 83–88, 2007.

[24] A. Matsunawa, J.-D. Kim, N. Seto, M. Mizutani, and S. Katayama, "Dynamics of keyhole and molten pool in laser welding," *J. Laser Appl.*, vol. 10, no. 6, p. 247, 1998.

[25] R. Xiao and X. Zhang, "Problems and issues in laser beam welding of aluminum-lithium alloys," *J. Manuf. Process.*, vol. 16, no. 2, pp. 166–175, 2014.

[26] W. E. King *et al.*, "Observation of keyhole-mode laser melting in laser powder-bed fusion additive manufacturing," *J. Mater. Process. Technol.*, vol. 214, no. 12, pp. 2915–2925, 2014.

[27] N. T. Aboulkhair, N. M. Everitt, I. Ashcroft, and C. Tuck, "Reducing porosity in AlSi10Mg parts processed by selective laser melting," *Addit. Manuf.*, vol. 1, pp. 77–86, 2014.

[28] P. A. Kobryn, E. H. Moore, and S. L. Semiatin, "Effect of laser power and traverse speed on microstructure, porosity, and build height in laser-deposited Ti-6Al-4V," *Scr. Mater.*, vol. 43, no. 4, pp. 299–305, 2000.

[29] R. C. Atwood, S. Sridhar, W. Zhang, and P. D. Lee, "Diffusion- Controlled Growth of Hydrogen Pores in Aluminium- Silicon Casting: In Situ Observation and Modelling," *Acta Mater.*, vol. 48, pp. 405–417, 2000.

[30] V. Khalajzadeh, K. D. Carlson, D. G. Backman, and C. Beckermann, "A Pore-Centric Model for Combined Shrinkage and Gas Porosity in Alloy Solidification," *Metall. Mater. Trans. A*, vol. 48, no. 4, pp. 1797–1816, 2017.

[31] K. D. Li and E. Chang, "Mechanism of nucleation and growth of hydrogen porosity in solidifying A356 aluminum alloy: An analytical solution," *Acta Mater.*, vol. 52, no. 1, pp. 219–231, 2004.

[32] J. Jakumeit, S. Jana, T. Waclawczyk, A. Mehdizadeh, A. Sadiki, and J. Jouani, "Four-phase fully-coupled mold-filling and solidification simulation for gas porosity prediction in aluminum sand

casting," *IOP Conf. Ser. Mater. Sci. Eng.*, vol. 33, no. 1, 2012.

[33] D. M. Stefanescu and a V Catalina, "Physics of microporosity formation in casting alloys – sensitivity analysis for Al–Si alloys," *Int. J. Cast Met. Res.*, vol. 24, no. 3/4, pp. 144–150, 2011.

[34] J. G. Kaufman and E. L. Rooy, *Aluminum Alloy Casting: Properties, Processes, and Applications*. ASM International, 2004.

[35] Q. Han and S. Viswanathan, "Hydrogen evolution during directional solidification and its effect on porosity formation in aluminum alloys," *Metall. Mater. Trans. A*, vol. 33, no. 7, pp. 2067–2072, 2002.

[36] J. Campbell, "Pore Nucleation in Solidifying Metals," *ISI Publ.*, vol. 110, pp. 18–26, 1968.

[37] J. A. Dantzig and M. Rappaz, *Solidification*. Boca Raton, FL: CRC Press Taylor and Francis Group, 2016.

[38] S. Kou, *Welding Metallurgy Second Edition*, vol. 822, no. 1–3. Hoboken, New Jersey: John Wiley and Sons, Inc., 2003.

[39] Y. Lee, "Simulation of Laser Additive Manufacturing and its Applications," pp. 1–215, 2015.

[40] N. T. Aboulkhair, I. Maskery, C. Tuck, I. Ashcroft, and N. M. Everitt, "On the formation of AlSi10Mg single tracks and layers in selective laser melting: Microstructure and nano-mechanical properties," *J. Mater. Process. Technol.*, vol. 230, pp. 88–98, 2016.

[41] V. A. Fassel and R. N. Kniseley, "Inductively coupled plasma. Optical emission spectroscopy," *Anal. Chem.*, vol. 46, no. 13, p. 1110A–1120a, 1974.

[42] K. Papp and E. Kovács-Csetényi, "Diffusion of hydrogen in solid aluminium," *Scr. Metall.*, vol. 11, no. 11, pp. 921–923, 1977.

[43] D. Rosenthal, "Mathmatical theory of heat distribution during welding and cutting.," *Weld. J.*, vol. 20, pp. 220–234, 1941.

[44] D. Rosenthal, "The theory of moving sources of heat and its application to metal treatments," *Trans. Am. Soc. Mech. Eng.*, vol. 68, pp. 849–866, 1946.

[45] G. P. Ivantsov, "Temperature field around the spherical, cylindrical, and needle-crystals which grow in supercooled melt.," *Dokl. Akad. Nauk. USSR*, vol. 58, no. 1113, 1947.

[46] A. Plotkowski *et al.*, "Evaluation of an Al-Ce Alloy for Laser Additive Manufacturing," *Acta Mater.*, vol. 126, pp. 507–519, 2016.

[47] M. Rappaz, J. M. Drezet, and M. Gremaud, "A new hot-tearing criterion," *Metall. Mater. Trans. A*, vol. 30, no. 2, pp. 449–455, 1999.

Appendix

```
 Analytical Solutal field solution.
clear all
clc
%Analytical Temperature or Concentration Solution for a paraboloid.
%Author: Travis McFalls
%2018 Masters Thesis UTK
%This program will calculate the dimensionless Temperature and concentration
%fields in-front of a 3D paraboloid simulating Cellular dendrite growth
%during solidification. This Analytical solution ignores the effects of
%Curvature and Kinetics.  This model is based upon the solutions found in
%the book "Solidification" By Dantzig, and Rappaz.
%

%% Sieverts Law calculation for the Equilibrium Concentration
% This is not necessary for the solution of the rest of the model.
T=850:.1:869;               %Temperature Vector
f=1.25;                     %Activity Coefficient
a1=2691.96;                 %Constant for Equilibrium Coefficient for H
% SR=4124;
% DH=3000;
% AH=4.11;
% eh=.03;
% rh=-.0008;
% fa=1.25*(10^(eh*.1+rh*(.1^2)));
b1a=1.32;                       % Secondary Constant for Equilibrium Coefficient for H
for i=1:length(T)
ke(i)=10^(-((a1/T(i))+b1a));          %Equilibrium Coefficient
Clpnew(i)=(ke(i)/f);                %Equilibrium Concentration Weight Percent
% wooptie(i)=AH^(-1/2)*exp(DH/(2*SR*T(i)));
Clpnew(i)=(Clpnew(i)*1e6)/100;
```

```
Clpnew1(i)=Clpnew(i)*1.12;            %Conversion to ml/100g units
end

%% Definition of Parameters from Cartesian coordinates to Paraboloidal (2 sets)

Rtip=1e-7;
Rtip2=1e-8;
v=.01;
v2=1;
r=0:.01e-6:5e-6;
vc=.5:.05:1.5;
z=(Rtip/2)-(r.^2/(2*Rtip));
z2=(Rtip2/2)-(r.^2/(2*Rtip2));
scalez=z/Rtip;
scalez2=z2/Rtip2;
scaler=r/Rtip;
%% Conversion of Cartesian to Paraboloidal
for i=1:length(r)
   for j=1:length(z)

      zeda(i,j)=sqrt(scalez(j)+sqrt(scaler(i)^2+scalez(j)^2));
      lumpi(i,j)=sqrt(-scalez(j)+sqrt(scaler(i)^2+scalez(j)^2));
      zeda2(i,j)=sqrt(scalez2(j)+sqrt(scaler(i)^2+scalez2(j)^2));
      lumpi2(i,j)=sqrt(-scalez2(j)+sqrt(scaler(i)^2+scalez2(j)^2));
   end
end
%% Solving for Peclet number and Boundary conditions of the thermal Boundary layer
alpha=7.10e-5;
Pe=(v*Rtip)/(2*alpha);
ste=(920*(19)/321000);
```

```
ste3=Pe*exp(Pe)*expint(Pe);                %Ivantsov solution

%% Conversion back to cartesian coordinates
for i=1:length(zeda)
   for j=1:length(lumpi)
      R(i,j)=zeda(i)*lumpi(j);
      Z(i,j)=.5*((zeda(i)^2)-(lumpi(j)^2));
   end
end
NegR=R*-1;
%% 2D and 3D Analyitcal Solution of the Non Dimensional temperature fields around a paraboliod
for i=1:length(zeda)
   theta2(i)=((sqrt(pi()*Pe))/ste)*exp(Pe)*erfc(zeda(i)*sqrt(Pe));
   theta3(i)=(expint(Pe*(zeda(i)^2)))/(expint(Pe));
end
%% Plotting of 3D Solutions
%Plots along lines chosen by user
%Values will change based upon the Peclet number and data plotted must be
%re-selected
hold on
plot(Z(1,:),R(1,:),'k','LineWidth',2.5)
h1=plot(Z(1,:),R(1,:),'k','LineWidth',2.5);
plot(Z(1,:),NegR(1,:),'k','LineWidth',2.5)

plot(Z(60,:),R(60,:),'--b','LineWidth',2.5)
h2=plot(Z(60,:),R(60,:),'--b','LineWidth',2.5);
plot(Z(60,:),NegR(60,:),'--b','LineWidth',2.5)

plot(Z(132,:),R(132,:),'--r','LineWidth',2.5)
h3=plot(Z(132,:),R(132,:),'--r','LineWidth',2.5);
```

```
plot(Z(132,:),NegR(132,:),'--r','LineWidth',2.5)

h4=plot(Z(485,:),R(485,:),'--m','LineWidth',2.5);
plot(Z(485,:),R(485,:),'--m','LineWidth',2.5);
plot(Z(485,:),NegR(485,:),'--m','LineWidth',2.5)

% h5=plot(Z(25,:),R(25,:),'--k');
% plot(Z(25,:),R(25,:),'--k')
% plot(Z(25,:),NegR(25,:),'--k')
%
% h6=plot(Z(44,:),R(44,:),'--y');
% plot(Z(44,:),R(44,:),'--y')
% plot(Z(44,:),NegR(44,:),'--y')

label0=strcat('\fontsize{25}Theta =', num2str(theta3(1),2));
label1=strcat('\fontsize{25}Theta =',num2str(theta3(60),2));
label2=strcat('\fontsize{25}Theta =',num2str(theta3(132),2));
label3=strcat('\fontsize{25}Theta =',num2str(theta3(485),2));
% label4=strcat('\fontsize{15}Theta =',num2str(theta3(25),2));
% label5=strcat('\fontsize{15}Theta =',num2str(theta3(44),2));
ylim([-3 3])
xlim([-6 10])
legend([h1 h2 h3 h4],label0,label1,label2,label3)
legend('show')
title('\fontsize{35}Dimentionless Temperature Profile')
xlabel('\fontsize{25}z/Rtip')
ylabel('\fontsize{25}r/Rtip')
set(gca,'Color',[0.8 0.8 0.8]);
dim1=[.2 .35 .3 .3];
b1=strcat('\fontsize{25}Pe=',num2str(Pe,3));
```

```
annotation('textbox',dim1,'String',b1,'FitBoxToText','on')

hold off

%% Set up for Solution of the Concentration fields around the paraboloid
T=850;
kH=.07;
D=3.8e-6;
a=2315;
Dh=D*exp(-a/T);
%% Solution for the Peclet number for both cases.
Pec=(v*Rtip)/(2*Dh);
Pec3=(v2*Rtip2)/(2*Dh);

%% Analytical solution of Dimensionless concentration fields around a 3D paraboloid
for i=1:length(zeda)

  Cl3(i)=(expint(Pec*(zeda(i)^2)))/(expint(Pec));
  Cl4(i)=(expint(Pec3*(zeda2(i)^2)))/(expint(Pec3));
end


%% Ivantsov solution for the Boundary Condition at the Liquid Solid Interface

stec13=Pec*exp(Pec)*expint(Pec);
stec14=Pec3*exp(Pec3)*expint(Pec3);
%% Setting up range of values for Plotting
X=-25:.01:25;
for i=1:length(X)
   y(i)=0;
```

```
end
%% Plotting Both cases for the Concentration fields around the 3D Paraboliod
figure(2)
hold on
plot(Z(1,:),R(1,:),'k','LineWidth',2.5)
h1=plot(Z(1,:),R(1,:),'k','LineWidth',2.5);
plot(Z(1,:),NegR(1,:),'k','LineWidth',2.5)

plot(Z(12,:),R(12,:),'--b','LineWidth',2.5)
h2=plot(Z(12,:),R(12,:),'--b','LineWidth',2.5);
plot(Z(8,:),NegR(8,:),'--b','LineWidth',2.5)

plot(Z(26,:),R(26,:),'--r','LineWidth',2.5)
h3=plot(Z(26,:),R(26,:),'--r','LineWidth',2.5);
plot(Z(15,:),NegR(15,:),'--r','LineWidth',2.5)

h4=plot(Z(92,:),R(92,:),'--m','LineWidth',2.5);
plot(Z(92,:),R(92,:),'--m','LineWidth',2.5);
plot(Z(36,:),NegR(36,:),'--m','LineWidth',2.5)

h5=plot(Z(308,:),R(308,:),'--k','LineWidth',2.5);
plot(Z(308,:),R(308,:),'--k','LineWidth',2.5)
plot(Z(82,:),NegR(82,:),'--k','LineWidth',2.5)

% h6=plot(Z(115,:),R(115,:),'--y','LineWidth',2.5);
% plot(Z(115,:),R(115,:),'--y','LineWidth',2.5)
% plot(Z(501,:),NegR(501,:),'--y','LineWidth',2.5)

plot(X,y,'k','LineWidth',3)
label0=strcat('\fontsize{25}Cl =', num2str(Cl3(1),2));
```

```
label1=strcat('\fontsize{25}Cl =',num2str(Cl3(12),2));
label2=strcat('\fontsize{25}Cl =',num2str(Cl3(26),2));
label3=strcat('\fontsize{25}Cl =',num2str(Cl3(92),2));
label4=strcat('\fontsize{25}Cl =',num2str(Cl3(308),2));
% label5=strcat('\fontsize{25}Cl =',num2str(Cl3(115),2));
ylim([-3 3])
xlim([-4 8])
legend([h1 h2 h3 h4 h5],label0,label1,label2,label3,label4)
legend('show')
xt = get(gca, 'XTick');
set(gca, 'FontSize', 15)
yt=get(gca,'Ytick');
set(gca,'FontSize',15)
% title('\fontsize{35}Dimensionless Hydrogen Concentration Profile')
xlabel('\fontsize{25}z/Rtip')
ylabel('\fontsize{25}r/Rtip')
set(gca,'Color',[0.8 0.8 0.8]);
dim1=[.2 .35 .3 .3];
dim2=[.2 .15 .3 .3];
b1=strcat('\fontsize{25}Pe=',num2str(Pec,3));
annotation('textbox',dim1,'String',b1,'FitBoxToText','on')

b2=strcat('\fontsize{25}Pe=',num2str(Pec3,3));
annotation('textbox',dim2,'String',b2,'FitBoxToText','on')
hold off


%% Solution of the supersaturation at the Boundary layer (liquid Solid interface)

ppm=4;
```

```
% CO=ppm*.04*(1/83.5);

CO=ppm*1.12;
ko=.07;
% for i=1:length(Pec2)
% Clstar(i)=CO/(1-(stec3(i)*(1-ko)));
% end
Clstar1=CO/(1-(stec13*(1-ko)));
Clstar2=CO/(1-(stec14*(1-ko)));

%% Solution of the solute field infront of the paraboloid
for i=1:length(Cl3)
   clnew(i)=Cl3(i)*(Clstar1-CO)+CO;
   clnew2(i)=Cl4(i)*(Clstar2-CO)+CO;
end

%% Conversion to cartesian coordiantes from Paraboloidal
for i=1:length(zeda)
   znew(i)=(zeda(i)^2)/2;
   znew2(i)=(zeda2(i)^2)/2;
end
%% Plotting concentration change as a function of distance infront of paraboloid tip for both conditions
figure(3)
hold on
% title('\fontsize{35}Concentration H infront of the dendrite tip')
plot(znew,clnew,'LineWidth',3.5)
plot(znew2,clnew2,'LineWidth',3.5)
xlabel('\fontsize{25}z/Rtip')
ylabel('\fontsize{25}H Concentration (ml/100g)')
label1=strcat('\fontsize{25}Bottom of weldpool Pe=',num2str(Pec,3));
```

```
label2=strcat('\fontsize{25}Rear of the weldpool Pe=',num2str(Pec3,3));
legend(label1,label2)
legend('show')
xt = get(gca, 'XTick');
set(gca, 'FontSize', 15)
yt=get(gca,'Ytick');
set(gca,'FontSize',15)
hold of
```

Vita

Travis McFalls was born in Knoxville, TN, to parents Robert and Vivian Mcfalls in 1986. He has one brother Jay Mcfalls and a spouse Simona. Simona and Travis have one daughter Olivia. Travis graduated highschool from Temple Baptist Academy and was a participant on both the baseball and basketball teams. After graduation he spent two years at Pellissippi State Community College and then transferred to the University of Tennessee Knoxville to finish out an Aerospace Engineering degree in 2010. He then started his own financial advisory firm in 2012 with a business partner Dan Brandfast. Travis left the business in 2016 to return to UTK as a graduate student pursuing a master's degree in mechanical engineering. He graduated in August 2018 and took a position with BWxT researching the additive manufacturing of refractory metals.